



Subjective confidence reflects representation of Bayesian probability in cortex

Laura S. Geurts¹, James R. H. Cooke¹, Ruben S. van Bergen^{1,2} and Janneke F. M. Jehee¹✉

What gives rise to the human sense of confidence? Here we tested the Bayesian hypothesis that confidence is based on a probability distribution represented in neural population activity. We implemented several computational models of confidence and tested their predictions using psychophysics and functional magnetic resonance imaging. Using a generative model-based decoding technique, we extracted probability distributions from neural population activity in human visual cortex. We found that subjective confidence tracks the shape of the decoded distribution. That is, when sensory evidence was more precise, as indicated by the decoded distribution, observers reported higher levels of confidence. We furthermore found that neural activity in the insula, anterior cingulate and prefrontal cortex was linked to both the shape of the decoded distribution and reported confidence, in ways consistent with the Bayesian model. Altogether, our findings support recent statistical theories of confidence and suggest that probabilistic information guides the computation of one's sense of confidence.

Virtually any decision comes with a sense of confidence—a subjective feeling that clearly affects our everyday choices. For example, we reduce speed when driving at night because we feel less confident about our estimates of distance to surrounding traffic, we hesitate to try a piece of food when unsure about its taste and we resist investing in stocks unless convinced of their likely future profit. But what is this sense of confidence that accompanies almost all of our decisions?

Recent Bayesian decision theories^{1–5} propose that confidence corresponds to the degree of belief, or probability, that a choice is correct based on the evidence. More specifically, these theories propose that confidence is a function of the posterior probability of being correct, which links confidence directly to the quality of the evidence on which the decision is based. Thus, greater imprecision in the evidence reduces the probability that the choice is correct, which should result in lower levels of confidence. The agent's evidence is similarly described as a degree of belief in an event, or more formally as a probability distribution over a latent variable. For example, the evidence could be a probability distribution over the perceived distance to surrounding traffic. The width of the distribution (the range of probable distances) is broader in the dark than on a clear day, thereby signalling greater imprecision or uncertainty. Although central to the Bayesian confidence hypothesis, whether such probabilistic representations play a role in confidence is currently unclear.

Results from behavioural studies^{6–9} are consistent with the notion that confidence is computed from the degree of imprecision in sensory information. However, a major limitation of this work has been the use of physical sources of noise, such as a variation in image brightness or contrast, to manipulate uncertainty. This is problematic because it could be that observers simply monitor such stimulus properties as external cues to uncertainty and confidence^{7,10–13}. While physiological studies have found neural correlates of statistical confidence in the orbitofrontal^{14,15} and lateral intraparietal cortex¹⁶, these studies used a two-alternative forced choice task, so that the animal could simply rely on the distance between stimulus estimates (that is, point estimates) and category boundary to compute

confidence¹⁷ and need not use a representation of probability. Thus, one of the most fundamental assumptions of normative theories of decision-making—that confidence is derived from a probabilistic representation of information—has yet to be tested in cortex.

Here we use a combination of functional magnetic resonance imaging (fMRI), psychophysics and computational modelling to address two fundamental questions. Is confidence based on a probabilistic representation of sensory information? And if so, what neural mechanisms extract confidence from this cortical representation of uncertainty? Human participants viewed random orientation stimuli and reported both the orientation of the stimulus and their level of confidence in this judgement. Critically, no physical noise was added to the stimuli. We quantified the degree of uncertainty associated with stimulus representations in visual cortex using a probabilistic decoding approach^{10,18}, relying on trial-by-trial fluctuations in internal noise to render the evidence more or less reliable to the observer. We used the decoded probability distributions to compare between human data and simulated data from a Bayesian observer, as well as two alternative models implementing heuristic strategies for confidence. Corroborating the Bayesian model, we discovered that human confidence judgements track the degree of uncertainty contained in visual cortical activity. That is, when the cortical representation of the stimulus was more precise (as indicated by a narrower decoded probability distribution), participants reported higher levels of confidence. In addition, activity in the dorsal anterior insula (dAI), dorsal anterior cingulate cortex (dACC) and rostralateral prefrontal cortex (rIPFC) reflected both this sensory uncertainty and reported confidence, in ways predicted by the Bayesian observer model. Taken together, these results support normative theories of decision-making and suggest that probabilistic sensory information guides the computation of one's sense of confidence.

Results

Ideal observer models. The observer's task is to infer the orientation of a stimulus from a noisy sensory measurement and to report both this estimate and their level of confidence in this judgement.

¹Donders Institute for Brain, Cognition and Behavior, Radboud University, Nijmegen, the Netherlands. ²Zuckerman Mind Brain Behavior Institute, Columbia University, New York, NY, USA. ✉e-mail: janneke.jehee@donders.ru.nl

We consider three model observers for this task. The decision process is identical for all three observers, but they use different strategies for confidence.

The observer's measurement m of the sensory stimulus s is corrupted by noise: even when the physical stimulus is held constant, the measurement varies from trial to trial. Thus, the relationship between stimulus and measurement on each trial is given by a probability distribution, $p(m|s)$, which we model as a circular Gaussian centred on the stimulus and with variance $\sigma_m^2(s)$. This variability in the measurements stems from various sources of noise that are of both sensory and non-sensory origin. Specifically, we consider three sources of noise: two sensory and one non-sensory. The first source depends on stimulus orientation, with larger noise levels for oblique than for cardinal stimulus orientations. This pattern captures the well-established 'oblique effect' in orientation perception^{19,20}. The second source varies in magnitude from trial to trial and captures, for example, random fluctuations in neural response gain in sensory areas²¹. Finally, non-sensory noise refers to those sources of variance that affect, for example, the stimulus representation while held in working memory, or task-related processes in areas downstream of sensory cortex.

To infer the orientation of the stimulus from the measurement, all three observers invert the generative model to compute the posterior probability distribution $p(s|m)$ (equation (12)). This distribution quantifies the degree to which different stimulus values are consistent with the measurement. The mean of the posterior distribution is the model observer's estimate of the stimulus \hat{s} . We take the (circular) variance of the distribution as a measure of the degree of uncertainty in this estimate. The observer's internal estimate of orientation is subsequently translated into an overt (behavioural) response, r . This transformation from internal estimate into motor response is noisy. Thus, across trials, the response fluctuates around \hat{s} , where (motor) noise is drawn from a circular Gaussian (equation (13)).

How does each of the observer models compute confidence? The ideal strategy is to consider the degree of imprecision in the observer's decision, which depends on all sources of variance that affect their reports. Specifically, for the estimation task used here, it is statistically reasonable to compute confidence as a function of the expected magnitude of the error in the observer's response. We quantified this as follows:

$$c_B = \frac{1}{\int p(s|m) \text{angle}(r,s)^2 ds} \quad (1)$$

where c_B refers to the reported level of confidence, and $\text{angle}(r,s)^2$ represents the magnitude of the response error (that is, the squared acute-angle distance between response and (latent) stimulus). In other words, when uncertainty in evidence is higher, the expected decision error tends to be larger, and reported confidence will be lower. However, our predictions do not strongly depend on the particular function assumed here, as long as confidence monotonically decreases when overall uncertainty increases. We refer to this model as the Bayesian observer, as confidence is based (in part) on the posterior probability distribution—a probabilistic notion of uncertainty.

The second model observer uses certain properties of the stimulus, such as its orientation, as a cue to confidence. This observer has learned through experience that behavioural precision is usually better for cardinal than for oblique orientations. The observer utilizes this learned relationship as a heuristic and simply reports lower levels of confidence for those orientations that generally result in reduced levels of performance. We refer to this model as the Stimulus heuristics observer and formally define their confidence as:

$$c_S = \frac{1}{f(\hat{s})} \quad (2)$$

where $f(\hat{s})$ is a function that rises for oblique orientations (see equation (14) in the Methods). As the strategy ignores many sources of noise that create uncertainty, it is clearly suboptimal, but it could potentially explain human behaviour, which is why we include the strategy here.

The third and final model observer ignores the imprecision in internal estimates altogether and computes confidence exclusively from the noise in their motor response. We refer to this model as the Response heuristics observer. That is, on a given trial, the observer simply notices a large offset between their internal orientation estimate and overt (motor) response. Observing that their response is off, they report lower levels of confidence. This is not an ideal strategy, but it could nonetheless result in a reliable link between confidence and behavioural performance, as we will show in our simulations below. We define confidence for this observer model as:

$$c_R = \frac{1}{\text{angle}(r,\hat{s})^2} \quad (3)$$

where $\text{angle}(r,\hat{s})^2$ is the squared acute-angle distance between orientation estimate \hat{s} and response r . Figure 1 summarizes the three observer models.

Model predictions. What behavioural patterns should one observe for the different strategies for confidence? To address this question, we simulated the behavioural orientation estimates and associated confidence reports of the three model observers. As we will show below, this leads to a set of concrete predictions that we can then test in psychophysical and neuroimaging experiments.

Does confidence predict behavioural performance? To address this question, we binned the simulated data according to reported level of confidence and calculated the across-trial variance in behavioural orientation estimates for each of the bins. We first did this irrespective of the orientation of the stimulus. We found that the orientation judgements of the model observers were generally more precise when confidence was higher, regardless of the strategy for confidence employed by the observer (Fig. 2a). Thus, a predictive link between confidence and behavioural precision is consistent with several strategies and does not necessarily imply that confidence is based on a probabilistic representation of the degree of uncertainty in one's evidence.

We next turned to the relationship between confidence and behavioural performance for a constant stimulus. Closely replicating the experimental analysis procedures (see below), we first removed the effect of stimulus orientation from confidence, binned the data according to residual level of confidence and calculated the variance in behavioural orientation estimates for each of the bins. We found that higher levels of confidence again predicted greater behavioural precision for both the Bayesian and Response heuristics models (Fig. 2b). For the Stimulus heuristics observer, in contrast, we observed no clear link between confidence and behavioural performance. This makes sense, as this observer uses orientation as a cue to confidence, so an identical orientation stimulus should, when averaged across repeated presentations, always result in the same level of confidence, irrespective of any stimulus-independent sources of variance. This analysis could thus enable us to differentiate between some, though not all, strategies for confidence.

We next considered the relationship between confidence and the quality of the observer's evidence. Specifically, we determined the extent to which the degree of uncertainty in their sensory evidence predicted reported levels of confidence. Sensory uncertainty was quantified as the width of a probability distribution (Methods), similar to the empirical conditions. For practical reasons, we here disregard the contribution of non-sensory sources of variance and focus on sensory uncertainty alone, so as to closely match the empirical analyses. The data were binned for visualization only, and the mean levels of confidence and uncertainty were computed

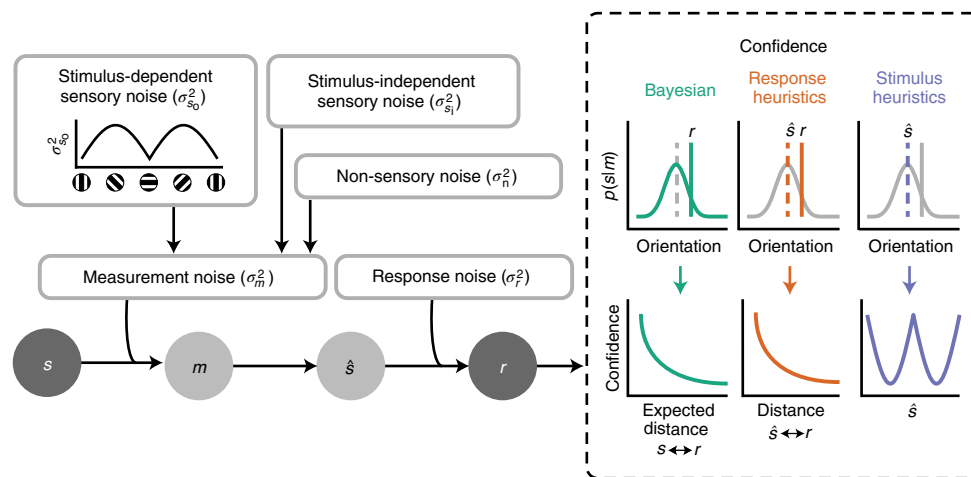


Fig. 1 | Overview of sources of noise and three observer models. The observers' task is to estimate the presented stimulus orientation s from a noisy measurement m . Multiple sources of noise affect the perceptual decision-making process. The measurements (m) vary from trial to trial due to sensory sources of noise, which can be decomposed into stimulus-related ($\sigma_{s_0}^2$) and stimulus-independent ($\sigma_{s_1}^2$) noise, as well as (unexplained) downstream (non-sensory) noise (σ_n^2). The observers compute their stimulus estimates \hat{s} as the mean of the posterior distribution $p(s|m)$. The internal orientation estimate is transformed into a behavioural (overt) response r , which is subject to further noise (σ_r^2). The observers also give their level of confidence in this behavioural estimate. The Bayesian observer computes confidence as a function of the expected distance between latent stimulus and response, which depends on both the response itself and the width of the posterior $p(s|m)$; this incorporates all sources of measurement noise. The Stimulus heuristics observer computes confidence as a function of their perceptual orientation estimate (\hat{s}). The Response heuristics observer computes confidence as a function of the distance between their internal orientation estimate (\hat{s}) and overt motor response (r). Both Heuristics observers ignore the degree of uncertainty in their orientation estimates when computing confidence.

for each of the bins. When analysed across stimulus orientations, and for both the Stimulus heuristics and Bayesian observers, the reported levels of confidence consistently decreased as sensory uncertainty increased. However, we observed no such relationship between confidence and uncertainty for the Response heuristics observer (Fig. 2c). When holding the stimulus constant, the results were even more distinct between confidence strategies. That is, after we removed the contribution of stimulus orientation (Methods), the relationship between sensory uncertainty and confidence still held for the Bayesian observer, but no such link between the fidelity of the observer's sensory representation and confidence was observed for the two remaining models (Fig. 2d). This illustrates the importance of considering internal levels of uncertainty when studying confidence and moreover indicates that these analyses, when combined, should enable us to adjudicate between strategies for confidence.

In sum, if human confidence estimates are based on probabilistic computations, then (1) behavioural variance in an orientation judgement task should be higher with reduced levels of confidence for a constant stimulus, (2) there should be an inverse relationship between sensory uncertainty in cortex and reported confidence, and (3) this inverse relationship should hold both across orientations and when holding the stimulus constant. With these predictions in hand, we now turn to the experimental data to see which strategy best describes human confidence judgements.

Human observers. Do human observers use a probabilistic representation of evidence quality when reporting confidence? To address this question, we presented 32 human participants with oriented gratings while we measured their brain activity using fMRI. The observers reported the orientation of the grating, as well as their confidence in this judgement (see Extended Data Fig. 1 for the trial structure). They generally performed well on this task, with a mean absolute behavioural estimation error of $4.34 \pm 0.212^\circ$ (mean \pm s.e.m. across participants).

We first focused on the link between behavioural performance and confidence. For each observer, we divided all trials, regardless of presented orientation, into ten bins of increasing confidence, and we computed and compared behavioural variability and mean level of confidence in each bin. We found a significant inverse relationship between confidence and behavioural variability ($t(287) = -16.79$; $P < 0.001$; $r = -0.70$; 95% confidence interval (CI), $(-0.76, -0.64)$; Fig. 3a, left). The observers' orientation judgements were thus more precise when confidence was high. This indicates that the participants were able to meaningfully estimate their own level of confidence in the task.

We next turned to the relationship between confidence and behavioural precision for repeated presentations of the same stimulus. For each observer, we again sorted the trials into ten bins of increasing confidence, calculated the mean level of confidence and behavioural variability across all trials in each bin, and computed the partial correlation coefficient between the two (while controlling for stimulus orientation; Methods). We considered two possible outcomes. If observers account for trial-by-trial fluctuations in internal noise when estimating confidence, as suggested by both the Bayesian and Response heuristics models, then higher levels of confidence should predict improved behavioural performance. If, in contrast, observers rely on orientation heuristics for confidence, then we should observe no systematic relationship between confidence and behavioural variability. The results revealed that behaviour was more precise when confidence was high (Fig. 3a, right; $t(286) = -11.02$; $P < 0.001$; $r = -0.55$; 95% CI, $(-0.62, -0.46)$). This is consistent with both the Bayesian and Response heuristics models and argues against an explanation of confidence in terms of orientation heuristics.

To adjudicate between the two remaining hypotheses, we then turned to the brain data. Specifically, we used a probabilistic decoding algorithm^{10,18} to characterize the degree of uncertainty in perceptual evidence from cortical activity patterns in areas V1–V3. Uncertainty in the cortical stimulus representation ('decoded

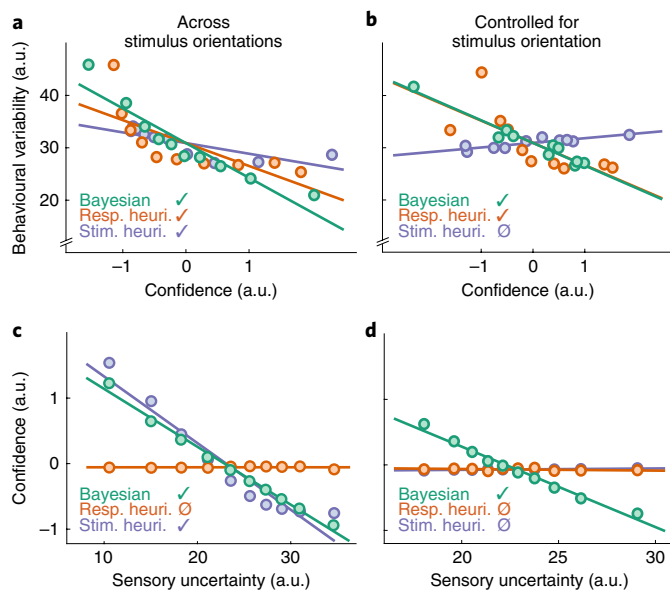


Fig. 2 | Ideal observer predictions. **a**, Relationship between confidence and behavioural variability for a uniform stimulus distribution (orientation range, 0–179°). The trials ($N = 50,000$) were binned into ten equal-sized bins of increasing confidence. For each bin, the variance of orientation estimation errors was computed and plotted against the mean level of confidence in that bin. The lines represent best linear fits. **b**, Same as **a**, but holding the stimulus constant. Confidence values were z-scored per observer such that they fall in the same range for all models. **c**, Relationship between sensory uncertainty and confidence for a uniform stimulus distribution (orientation range, 0–179°). For visualization purposes, the trials were binned into ten equal-sized bins of increasing uncertainty. The means of both confidence and sensory uncertainty were computed across all trials in each bin and are shown in the plot. The lines represent linear best fits computed on single-trial (unbinned) data. **d**, Same as **c**, but controlled for stimulus orientation. In **a–d**, the insets indicate, for each model, whether there is a relationship between the plotted variables (✓) or not (○). For ease of exposition, the group mean was added to the residuals plotted in **b,d**.

uncertainty’) was quantified on a trial-by-trial basis as the width (variance) of a decoded probability distribution (Methods). Benchmark analyses verified that (1) orientation decoding performance was well above chance levels (Extended Data Fig. 2a; see also ref.¹⁰), (2) decoded uncertainty was lower for cardinal than for oblique stimuli (Extended Data Fig. 2b; see also ref.¹⁰) and (3) decoded uncertainty predicted behavioural variability, both within and across stimulus orientations (Extended Data Fig. 2c,d; see also ref.¹⁰). Altogether, this confirms that the precision of the observer’s internal sensory evidence was reliably extracted from the patterns of fMRI activity on a trial-by-trial basis.

Do human observers rely on the quality of their internal visual evidence when estimating confidence? To address this question, we computed, for each individual observer, the trial-by-trial rank correlation coefficient (ρ) between reported confidence and decoded uncertainty (see Fig. 3b for an example observer). The obtained correlation coefficients were subsequently averaged across observers. Per our simulations, we predicted that if confidence is based on sensory uncertainty, then the imprecision in the observer’s sensory evidence, as assessed by the decoder, should predict the confidence judgements of the observer. If, however, confidence is consistent with heuristic computations based on non-sensory sources of noise, then we should observe no relationship between decoded uncertainty and reported confidence. Corroborating the Bayesian model,

there was a reliable inverse relationship between decoded uncertainty and behavioural confidence ($z = -2.17$; $P = 0.015$; $\rho = -0.018$; 95% CI, $(-0.035, -0.0018)$; Fig. 3c, left). To further substantiate this result, we repeated the analysis while controlling for stimulus orientation (Methods, see Extended Data Fig. 3 for fitted functions). This did not significantly reduce the strength of the observed relationship between the fidelity of the cortical stimulus representation and reported confidence ($z = 0.45$; $P = 0.33$; Cohen’s $q = 0.0054$; 95% CI, $(-0.018, 0.029)$; Fig. 3c, right) and again reached significance when using smaller numbers of voxels, which respond more strongly to the visual stimulus (Extended Data Fig. 4). Thus, when the cortical representation of a stimulus is more precise, observers consistently report higher levels of confidence, as predicted by the Bayesian model (and neither of the other models). Control analyses verified that these results were robust to variations in the number of voxels selected for analysis (Extended Data Fig. 4) and, moreover, that they could not be explained by eye movement, position or blinks, or by the mean amplitude of the blood-oxygen-level-dependent (BOLD) signal (Extended Data Fig. 5). Taken together, these results suggest that human observers rely on a probabilistic representation of the quality of their sensory evidence when judging confidence.

Sensory uncertainty and confidence in downstream areas. To further test the probabilistic confidence hypothesis, we next asked which downstream regions might read out the uncertainty contained in visual cortical activity to compute confidence. On the basis of our modelling work, we reasoned that if confidence is based on a probabilistic representation of the evidence, then we should be able to find downstream areas whose activity reflects sensory uncertainty and predicts reported confidence on a trial-by-trial basis. Specifically, we predicted an inverse relationship in activity between sensory uncertainty and confidence for these regions (Fig. 2d). Thus, under the probabilistic confidence hypothesis, cortical activity should not only increase (decrease) with reduced reliability of the observer’s perceptual evidence but also decrease (increase) when the observer reports greater levels of decision confidence.

We first focused on those areas that are driven by internal fluctuations in perceptual uncertainty. To identify candidate areas, we performed a whole-brain search. Specifically, we ran a general linear model (GLM) analysis in which we modelled the BOLD signal as a function of the degree of uncertainty decoded from visual cortical representations (in areas V1–V3), while controlling for differences in stimulus orientation (see Methods for further details). We found several clusters downstream of visual cortex where neural activity reliably co-fluctuated with trial-by-trial changes in decoded sensory uncertainty (see Fig. 4a for an overview, Supplementary Data for whole-brain maps and Supplementary Table 1 for a list of clusters). These included the dAI, dACC and left rIPFC—regions that are commonly associated with uncertainty²² (dAI), volatility^{23,24} (dACC) and metacognition²⁵ (rIPFC).

We next asked whether these uncertainty-tracking regions would also show a reliable opposite relationship to confidence in their activity, as predicted by the Bayesian observer model. To address this question, we performed region-of-interest (ROI) analyses within the candidate regions identified by the above whole-brain analysis. First, individual ROIs were created by selecting all uncertainty-driven voxels within predefined anatomical masks corresponding to dAI²⁶, dACC²⁷ and left rIPFC²⁸, using a leave-one-participant-out cross-validation procedure to avoid double-dipping^{29,30} (see Methods for the details and Extended Data Fig. 6 for the remaining clusters). For each participant, we then averaged the BOLD signal across all voxels within the ROI. To test whether BOLD activity was reliably modulated by the level of confidence reported by the observer, we performed a GLM analysis (see Methods for the model details). This revealed a significant effect of confidence on BOLD activity in all three regions (dAI:

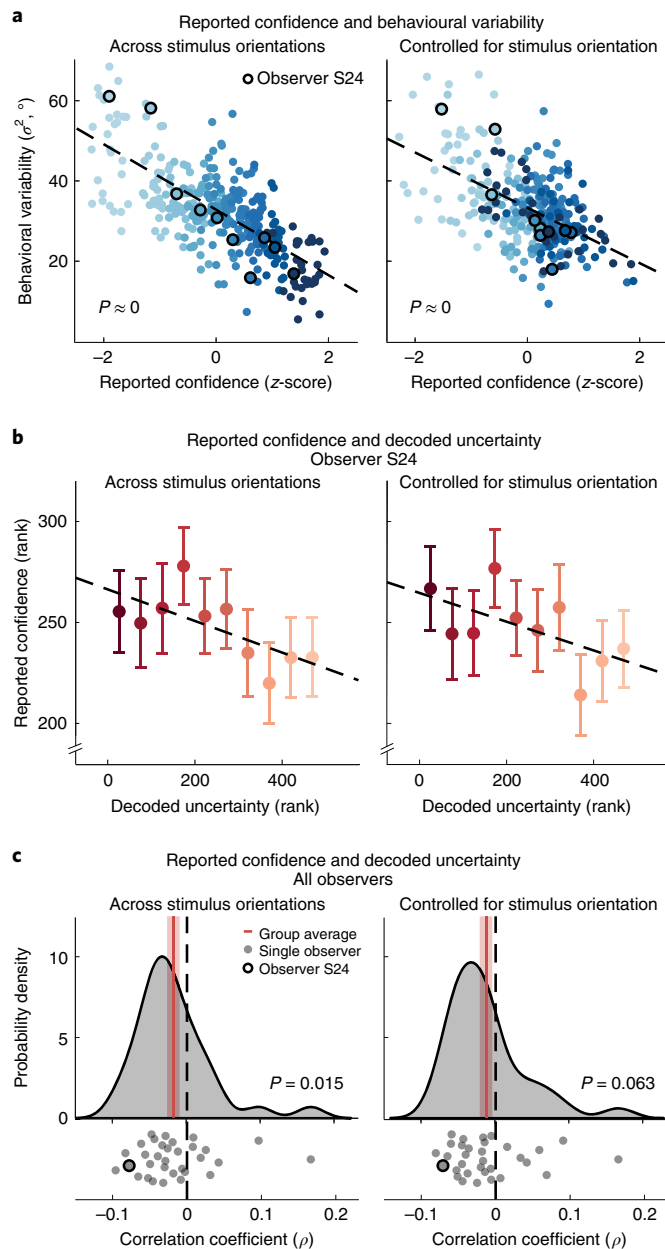


Fig. 3 | Reported confidence, behavioural variability and decoded sensory uncertainty. **a**, Behavioural variability decreases as confidence increases (left: $t(287) = -16.79$; $P < 0.001$; $r = -0.70$; 95% CI, $(-0.73, -0.67)$; right: $t(286) = -11.02$; $P < 0.001$; $r = -0.55$; 95% CI, $(-0.62, -0.46)$). The shades of blue indicate ten within-observer bins of increasing confidence. The dots represent single observers ($N=32$). For ease of exposition, the group mean was added to the plotted residuals. **b,c**, Decoded sensory uncertainty reliably predicts reported confidence. In **b**, the results for an example observer (S24) are shown (left: $z = -1.67$; $P = 0.047$; $\rho = -0.078$; 95% CI, $(-0.17, 0.014)$; right: $z = -1.52$; $P = 0.064$; $\rho = -0.071$; 95% CI, $(-0.16, 0.021)$). The analyses were performed on trial-by-trial data ($N = 493$); the data were binned (ten bins) for visualization only. The error bars represent ± 1 s.e.m. In **c**, the group average (red line; the shaded area represents ± 1 s.e.m.), probability density and individual correlation coefficients (left: $z = -2.17$; $P = 0.015$; $\rho = -0.018$; 95% CI, $(0.035, -0.0018)$; right: $z = -1.53$; $P = 0.063$; $\rho = -0.013$; 95% CI, $(-0.030, 0.0036)$) are shown. The grey dots indicate observers ($N = 32$); the circle denotes S24.

$F(3,93) = 25.94$; $P < 0.001$; $R^2 = 0.26$; 95% CI, $(0.12, 0.41)$; dACC: $F(3,93) = 27.33$; $P < 0.001$; $R^2 = 0.25$; 95% CI, $(0.10, 0.39)$; rLPFC: $F(3,90) = 2.88$; $P = 0.040$; $R^2 = 0.01$; 95% CI, $(-0.03, 0.05)$). It thus seems that neural activity in dAI, dACC and rLPFC is affected by both the trial-by-trial imprecision in sensory evidence and the level of confidence reported by the observers.

Having established that activity in dAI, dACC and rLPFC is modulated by confidence, we next investigated the hypothesized inverse relationship between sensory uncertainty and reported confidence on the cortical response in these regions. To illustrate our approach, we first focus on a single ROI (dAI; Fig. 4b). We computed, for each observer, the trial-by-trial correlation coefficient between decoded uncertainty and mean BOLD amplitude within the ROI (after removing the effect of stimulus orientation (Methods); see Fig. 4c for an example observer), averaged the coefficients across observers (Fig. 4d) and repeated the analysis over time (Fig. 4e, left). We also performed the same analysis for reported confidence (Fig. 4b–e) and for dACC and rLPFC (Fig. 4e). We discovered, in all three ROIs, a significant positive relationship between decoded uncertainty and cortical activity that was sustained over an extended period (Fig. 4e; all $P < 0.05$, family-wise error rate (FWER) controlled). Critically, the effect on the cortical response was reversed for confidence (Fig. 4e) and similarly held up over time (all $P < 0.05$, FWER-controlled). Thus, while the cortical response in dAI, dACC and rLPFC reliably increased with decoded uncertainty, activity in these regions consistently decreased with reported confidence, further corroborating the Bayesian confidence hypothesis. These effects could not be explained by trial-by-trial fluctuations in the participant's response time (see Extended Data Fig. 7 for control analyses). Especially interesting is that (in dACC and dAI) the positive correlation with uncertainty temporally preceded the negative correlation with reported confidence (dAI: $t(31) = -3.05$; $P = 0.005$; $d = -0.54$; 95% CI, $(-0.90, -0.17)$; dACC: $t(31) = -2.72$; $P = 0.011$; $d = -0.39$; 95% CI, $(-0.75, -0.032)$; rLPFC: $t(30) = -1.09$; $P = 0.29$; $d = -0.20$; 95% CI, $(-0.57, 0.17)$). Factoring in the (approximately four-second) haemodynamic delay inherent in the BOLD response, the effect of sensory uncertainty seems to be roughly time-locked to the presentation (and neural processing) of the stimulus, while the correlation with reported confidence coincides with the time when participants had to estimate their confidence. These distinct latencies further suggest that decoded uncertainty and reported confidence exert (partially) independent effects on activity in these regions, which was confirmed by a partial correlation analysis (Extended Data Fig. 8). Moreover, cortical activity in all three regions was additionally found to mediate the trial-by-trial relationship between decoded uncertainty and reported confidence (Extended Data Fig. 9). This indicates that some of the variance in cortical activity is shared between sensory uncertainty and subjective confidence, and alludes to a direct functional role of these regions in the computation of confidence from sensory uncertainty. Taken together, these results are consistent with the Bayesian confidence hypothesis and suggest that dAI, dACC and rLPFC are involved in the computation of confidence from a probabilistic representation of the quality of the observer's sensory evidence.

Discussion

What computations give rise to the subjective sense of confidence? Here we tested the Bayesian hypothesis that confidence is computed from a probabilistic representation of information in cortex. We first implemented a Bayesian observer model as well as two models using alternative strategies for confidence. This resulted in a set of predictions that we tested using psychophysics and fMRI. Corroborating the Bayesian model, we found that reported confidence reflects behavioural precision, even when stimulus properties such as orientation are held constant. Moreover, probability distributions decoded from population activity in visual cortex predict

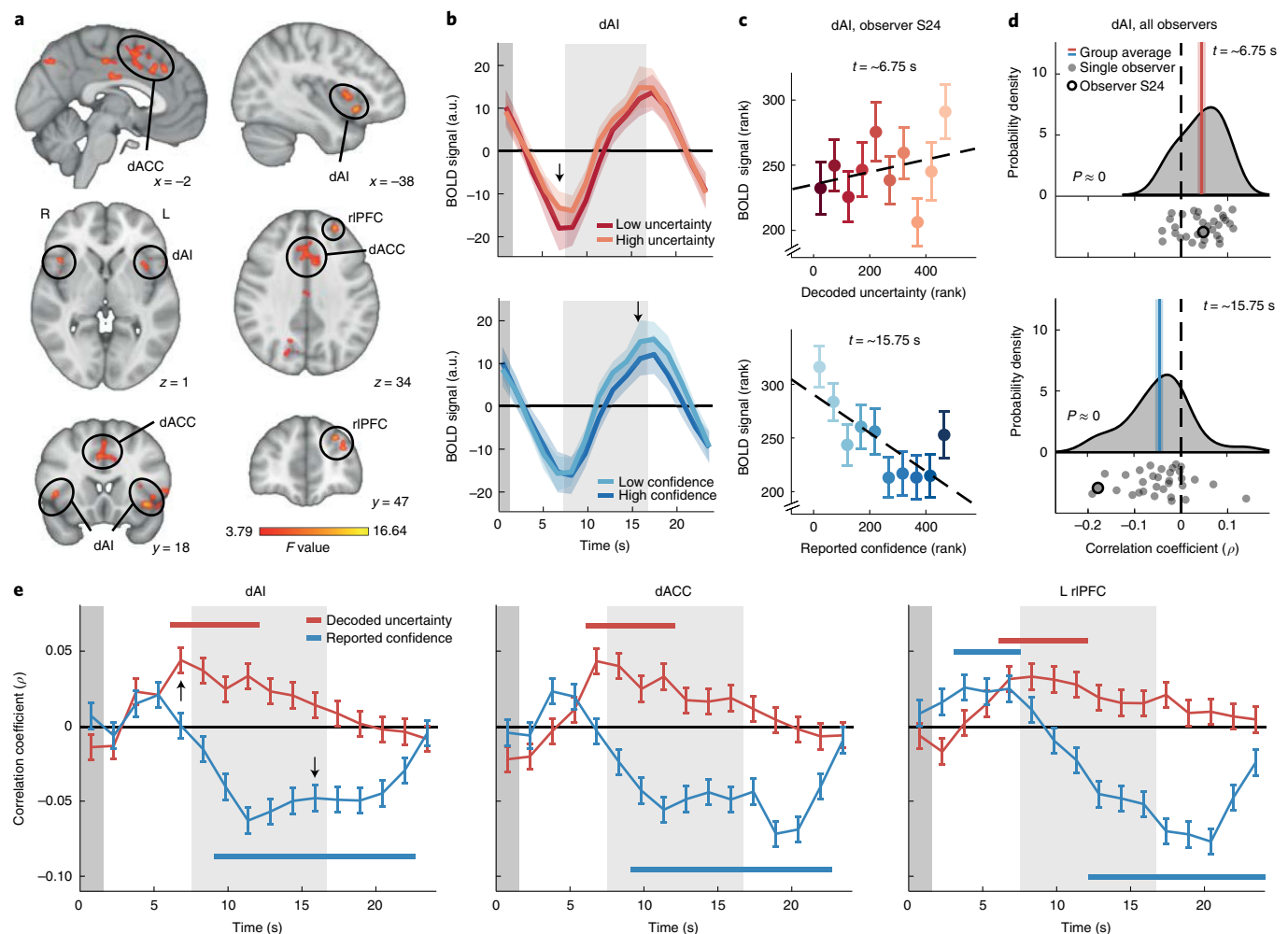


Fig. 4 | Activity in dAI, dACC and left rIPFC over time. a, Downstream clusters significantly modulated by uncertainty decoded from visual cortex ($P < 0.05$, FWER-controlled) (the data were masked to exclude occipital cortex; Supplementary Table 1 gives an overview of all activations, and see Supplementary Data for whole-brain maps). **b**, Cortical response in dAI for high versus low decoded uncertainty (top) and high versus low reported confidence (bottom), averaged across all observers. The trials were binned by a median split per observer. The black arrows indicate the data presented in **c** and **d**. **c**, Example observer S24. The observer's cortical response tentatively increases with decoded uncertainty and decreases with reported confidence. The trials ($N = 493$) were binned (ten bins) for visualization only; correlation coefficients were computed from trial-by-trial data. **d**, Group average (red or blue line) and correlation coefficients for individual observers (grey dots; $N = 32$). Shown is the relationship between cortical response amplitude and decoded uncertainty (top) or reported confidence (bottom). Both effects are statistically significant (permutation test; uncertainty: $\rho = 0.044$, $P < 0.001$; confidence: $\rho = -0.047$, $P < 0.001$). **e**, Group-averaged correlation coefficient between cortical response amplitude and decoded uncertainty (red) or reported confidence (blue). The horizontal lines indicate statistical significance ($P < 0.05$, FWER-controlled). The arrows indicate the data in **d**. In **b–e**, the dark grey area marks the stimulus presentation window, and the light grey area represents the response window. In **b–e**, the shaded areas and error bars denote ± 1 s.e.m.

the level of confidence reported by the participant on a trial-by-trial basis. We furthermore identified three downstream regions, dACC, dAI and rIPFC, where BOLD activity is linked to both the width of the decoded distributions and reported confidence in ways consistent with the Bayesian observer model. Taken together, these findings support recent normative theories and suggest that probabilistic information guides the computation of one's sense of confidence.

Earlier work on statistical confidence has manipulated evidence reliability by varying physical properties of the stimulus, such as its contrast. This left open the possibility that observers simply monitor these image features as a proxy for uncertainty^{7,10–12}, without considering an internal belief distribution over the latent variable. For this reason, we held the stimulus properties constant, relied on fluctuations in internal noise and extracted probability distributions directly from cortical activity. Our work shows that the uncertainty decoded from visual activity predicts the level of

confidence reported by the observer. No less important, we find that downstream regions commonly associated with volatility in the environment^{23,24}, decision-making^{22,31} and confidence^{25,32,33} represent trial-by-trial fluctuations in both this decoded uncertainty and reported confidence. Altogether, this strongly suggests that a probabilistic representation of information, and not stimulus heuristics or point estimates, drives human confidence reports.

While decision confidence is usually studied in the context of binary decisions, we here focused on a continuous estimation task, which requires observers to reproduce a feature of the stimulus. For binary decisions, confidence is normatively defined as a function of the observer's measurement and decision boundary, in addition to sensory uncertainty, and each of these parameters can vary on a trial-by-trial basis due to internal noise. For the continuous estimation task used here, confidence is more straightforwardly defined as a function of sensory uncertainty, without

many additional parameters. This definition makes this task ideally suited for addressing the probabilistic confidence hypothesis. While we specifically focused on uncertainty in continuous estimation, it seems nonetheless likely that the probabilistic nature of the representation will extend to binary choices and other decisions of increasing complexity.

Our findings are also important for understanding how uncertainty is represented in cortex. Previous work has shown that the width of the decoded probability distribution predicts the magnitude of behavioural orientation biases¹⁰, serial dependence effects in perception³⁴ and classification decisions³⁵. The current work extends these earlier findings by linking the decoded distributions directly to activity in downstream decision areas and the subjective level of confidence reported by the observer. Taken together, these findings suggest that probability distributions are not only represented in neural population activity but also used in the brain's computations.

Earlier work has implicated the involvement of the dACC, dAI and rLPFC in experimental (objective) manipulations of evidence reliability^{23,33,36–38}. Our results suggest that these regions similarly track spontaneous (internal) fluctuations in uncertainty and moreover mediate the link between sensory uncertainty and reported confidence, further elucidating their functional role in human decision-making. It thus seems that a more general notion of uncertainty is represented in these regions, albeit for different functional purposes. While the representation in dACC may serve to inform internal models and response selection^{39–42}, it seems likely that dAI integrates uncertainty with interoceptive and affective information to form a general subjective feeling state²², and rLPFC probably plays a key role in the integration of internal uncertainty with contextual information to compute confidence^{32,36,43–45}.

While we focused here on the link between subjective confidence and the precision of early sensory evidence in visual areas, confidence should additionally reflect uncertainty added by later stages of processing—for instance, when the item is held in visual working memory before observers make their judgement (although the impact of memory imprecision might be relatively small⁴⁶). Indeed, our ideal observer model incorporates these sources of variance in its estimates of confidence (equations (1), (8) and (9), σ_n^2). Given the involvement of early visual areas in visual working memory^{47,48}, this predicts that the imprecision in the visual cortical representation during the delay period between stimulus presentation and response should predict the level of confidence reported by the observer. Interestingly, additional analysis of the empirical data revealed that uncertainty decoded from signals during the retention interval indeed reliably predicted subjective levels of confidence (Extended Data Fig. 10). Although our design does not warrant strong conclusions regarding the nature of these signals (see Extended Data Fig. 10 for a discussion), these findings are consistent with a model that considers additional sources of variance when judging confidence. Corroborating this interpretation, a very recent study used our probabilistic decoding techniques and found that decoded uncertainty predicted the observer's judgements of uncertainty in a visual working memory task⁴⁹. It will be interesting for future work to further disentangle these and other sources of noise that affect the observer's decisions and associated levels of confidence.

In conclusion, we showed that behavioural confidence tracks the degree of uncertainty contained in neural population activity in visual cortex, suggesting that human observers have access to and can report about the degree of imprecision in their visual cortical representations of the stimulus. Furthermore, activity in the dACC, dAI and rLPFC is modulated by both this uncertainty and reported confidence in ways predicted by the Bayesian model, suggesting that these regions are involved in the computation of confidence from sensory uncertainty. Taken together, our results support recent normative theories of confidence and suggest that the subjective

feeling of confidence is based on a statistical measure of the quality of one's evidence.

Methods

Participants. Thirty-two healthy adult volunteers (age range 19–31, 20 female, 12 male) with normal or corrected-to-normal vision participated in this study. The sample size ($N=32$) was based on a power calculation (power = 0.8; $\alpha=0.05$). All participants gave informed written consent prior to their participation and received monetary compensation (eight and ten euros per hour for the behavioural and fMRI sessions, respectively). The study was approved by the local ethics committee (CMO Arnhem-Nijmegen, the Netherlands). Participants were included on the basis of their ability to perform the task, which was assessed in a separate behavioural training session before the experimental sessions.

Imaging data acquisition. The MRI data were acquired on a Siemens 3T MAGNETOM PrismaFit scanner at the Donders Center for Cognitive Neuroimaging, using a 32-channel head coil. For anatomical reference, a high-resolution T1-weighted image was collected at the start of each session (3D MPRAGE; repetition time (TR), 2,300 ms; inversion time (TI), 1,100 ms; echo time (TE), 3 ms; flip angle, 8 degrees; field of view (FOV), 256 mm × 256 mm; 192 sagittal slices; 1-mm isotropic voxels). B0 field inhomogeneity maps (TR, 653 ms; TE, 4.92 ms; flip angle, 60 degrees; FOV, 256 mm × 256 mm; 68 transversal slices; 2-mm isotropic voxels; interleaved slice acquisition) were acquired. Functional data were acquired using a multi-band accelerated gradient-echo EPI protocol, in 68 transversal slices covering the whole brain (TR, 1,500 ms; TE, 38.60 ms; flip angle, 75 degrees; FOV, 210 mm × 210 mm; 2-mm isotropic voxels; multiband acceleration factor, 4; interleaved slice acquisition).

Experimental design and stimuli. The participants performed an orientation estimation task while their cortical activity was measured with fMRI. They completed a total of 22–26 task runs, divided over two scan sessions on separate days. Prior to the experimental sessions, the participants extensively practised the task (two to four hours) in a separate behavioural session.

Throughout each task run, the participants fixated a bull's-eye target (radius, 0.375 degrees) presented at the centre of the screen. Each run consisted of 20 trials (16.5 s each), separated by an intertrial interval of 1.5 s, and started and ended with a fixation period (duration at the start, 4.5 s; at the end, 15 s). Each trial started with the presentation of the orientation stimulus, which remained on the screen for 1.5 s. This was followed by a 6-s fixation interval and then two successive 4.5-s response windows (Extended Data Fig. 1). The orientation stimuli were counterphasing sinusoidal gratings (contrast, 10%; spatial frequency, one cycle per degree; randomized spatial phase; 2-Hz sinusoidal contrast modulation) presented in an annulus around fixation (inner radius, 1.5 degrees; outer radius, 7.5 degrees; grating contrast decreased linearly to 0 over the inner and outer 0.5 degrees of the radius of the annulus). The stimulus orientations were drawn (pseudo)randomly from a uniform distribution covering the full orientation space (0–179 degrees) to ensure an approximately even sampling of orientations within each run. At the start of the first response window, a black bar (length, 2.8 degrees; width, 0.1 degrees; contrast, 40%) appeared at the centre of the screen at an initially random orientation. The participants reported the orientation of the previously seen grating by rotating this bar, using separate buttons for clockwise and counterclockwise rotation on an MRI-compatible button box. At the start of the second response window, a black bar of increasing width (contrast, 40%; bar width, 0.1–0.5 degrees, linearly increasing) and wrapped around fixation (radius, 1.4 degrees) became visible at the centre of the screen. The participants indicated their confidence in their orientation judgement by moving a white dot (contrast, 40%; radius, 0.05 degrees) on this continuous confidence scale, using the same buttons for clockwise and counterclockwise as for their orientation response. The mapping of confidence level to scale width (that is, whether the narrow end of the scale indicated high or low confidence) was counterbalanced across participants. The scale's orientation and direction (that is, width increasing in a clockwise or counterclockwise direction), as well as the starting position of the dot, were randomized across trials. For both response windows, the bar (scale) disappeared gradually over the last 1 s of the response window to indicate the approaching end of this window. Shortly before trial onset (0.5 s), the fixation bull's-eye briefly turned black (duration, 0.1 s) to indicate the start of the trial. Because we were interested in the effects of sensory uncertainty on cortical activity and confidence, rather than the cortical representation of confidence per se, and because reward-related signals might contaminate the representation of sensory information in visual areas⁵⁰, the participants received no trial-by-trial feedback about the accuracy of their judgements.

Each scan session also included one or two functional localizer runs, during which flickering checkerboard stimuli were presented in seven 12-s blocks interleaved with fixation blocks of equal duration. The checkerboard stimuli were presented within the same aperture as the grating stimuli (contrast, 100%; flicker frequency, 10 Hz; check size, 0.5 degrees). Retinotopic maps of the visual cortex were acquired in a separate scan session using standard retinotopic mapping procedures^{51–53}.

All visual stimuli were generated on a Macbook Pro computer using MATLAB and the Psychophysics Toolbox⁵⁴ and were presented on a rear-projection screen using a luminance-calibrated EIKI LC-XL100 projector (screen resolution, 1,024 × 768 pixels; refresh rate, 60 Hz). The participants viewed the screen through a mirror mounted on the head coil.

Behavioural data analysis. In general, the participants finished adjusting their orientation and confidence responses well before the end of the response windows (4.5 s each), taking on average $2,761 \pm 378$ ms (mean \pm s.d. across observers) for the orientation response and $2,587 \pm 313$ ms for the confidence response. Trials on which participants did not finish their response by the end of the response window were excluded from further analyses (0–43 of 440–520 trials). The error in the observer's behavioural orientation response was computed as the acute-angle difference between the reported and the presented orientation on a given trial. Orientation-dependent shifts (biases) in mean behavioural error were removed by fitting two fourth-degree polynomials to each observer's behavioural errors as a function of stimulus orientation (see ref. ¹⁰ for a similar procedure). One polynomial was fit to trials for which the presented stimulus orientation was between 90 and 179 degrees, and the second polynomial was fit to trials on which the presented stimulus orientation was between 0 and 89 degrees. We used the bias-corrected behavioural errors (that is, the residuals of this fit) in subsequent analyses. Behavioural errors that were more than three standard deviations away from the mean of each participant (after bias correction) were marked as guesses and excluded from further analysis (1–7 of 440–520 trials). To remove potential session-specific and participant-specific differences in usage of the confidence scale, confidence ratings were *z*-scored within sessions.

Preprocessing of MRI data. The raw functional imaging data were motion-corrected with respect to the middle volume of the middle run of the session, using FSL's MCFLIRT⁵⁵. The functional data were corrected for distortion using the within-session B0 field map and aligned to the T1-weighted image obtained during the same scan session. This anatomical (T1-weighted) image was aligned with a participant-specific unbiased template image, created by combining the T1-weighted images from the two sessions, using Freesurfer's *mri_robust_template*⁵⁶. Slow drifts in the BOLD signal were removed using FSL's nonlinear high-pass temporal filter with a sigma of 24 TRs (two trials), corresponding to a cut-off period of approximately 83 s.

For all univariate analyses, additional preprocessing steps were performed before high-pass filtering. Specifically, non-brain structures were removed using FSL's BET⁵⁷, and the data were spatially smoothed with a 6-mm Gaussian kernel using FSL's SUSAN⁵⁸. As the univariate analyses required combining data across participants, each participant's anatomical template image was nonlinearly registered to MNI152 space using FSL's FNIRT with a warp resolution of 10 mm isotropic⁵⁹.

A set of nuisance regressors was used to remove residual motion effects and global fluctuations in the BOLD signal. Per session, we defined an intercept regressor per run, 24 motion regressors based on the motion parameters estimated by MCFLIRT (all analyses) and two regressors reflecting the average signal in cerebrospinal fluid (CSF) and white matter (WM) (univariate analyses only). The CSF and WM regressors served to capture global fluctuations in signal intensity and were obtained by first creating WM and CSF masks based on the participant's anatomical scan data using FSL's FAST⁶⁰, and then removing the outer edges from these masks to exclude voxels at the tissue boundaries. For the multivariate and ROI-based univariate analyses, nuisance signals were removed from the BOLD signal prior to further analyses. For the whole-brain univariate analysis, motion, CSF/WM and intercept regressors were included as covariates in the GLM ('Whole-brain analysis').

For the multivariate analyses, the ROI (consisting of V1, V2 and V3) was identified on the reconstructed cortical surface. Within this ROI, and in the native space of each participant, we selected for further analysis the 2,000 voxels that were activated most strongly by the functional localizer stimulus while surviving a lenient statistical threshold ($P < 0.01$, uncorrected). Control analyses verified that our results were not strongly affected by the number of voxels selected for analysis (Extended Data Fig. 4). The time series of each selected voxel was subsequently *z*-normalized with respect to corresponding trial time points in the same run. Activation patterns for each trial were obtained by averaging over the first 3 s of each trial, after adding a 4.5-s temporal shift to account for haemodynamic delay. This relatively short time window was chosen to ensure that activity from the behavioural response window was excluded from analysis. For the control analyses in Extended Data Fig. 5, mean BOLD intensity values were calculated by averaging the *z*-normalized activation values across the selected voxels and time window. The results in Extended Data Fig. 10 were obtained using a sliding window of size 3 s (two TRs), chosen to match the window size of the main analysis. For each window of analysis, the *z*-normalized activation values were averaged and subsequently fed to the decoding algorithm.

Multivariate analysis (visual cortex). *Decoding algorithm.* Trial-by-trial uncertainty in cortical stimulus representations was computed using a generative model-based, probabilistic decoding algorithm^{10,18}, applied to selected voxels

in visual cortex (see the previous section for the voxel selection criteria). The model describes the generative distribution of the voxel activity patterns given a certain stimulus, $p(\mathbf{b}|s)$ —in other words, the probability that stimulus s will evoke activation pattern \mathbf{b} . The model assumes that, across trials, voxel activity follows a multivariate normal distribution around the voxel's tuning curve for orientation. Voxel tuning curves are defined as a linear combination $\mathbf{W}\mathbf{f}(s)$ of eight bell-shaped basis functions, each centred on a different orientation⁶¹:

$$f_k(s) = \max \left[0, \cos \left(2\pi \frac{s - \varphi_k}{180} \right) \right]^5 \quad (4)$$

where s is the orientation of the presented stimulus and φ_k is the preferred orientation of the k th population. The basis functions were spaced equally across the full orientation space (0–179 degrees) with the first centred at zero degrees. W_{ik} is the contribution of the k th basis function to the response of the i th voxel.

The covariance around the voxel tuning curves is described by the noise covariance matrix Ω :

$$\Omega = \rho \boldsymbol{\tau} \boldsymbol{\tau}^T + (1 - \rho) \mathbf{I} \circ \boldsymbol{\tau} \boldsymbol{\tau}^T + \sigma^2 \mathbf{W} \mathbf{W}^T \quad (5)$$

The first term of this covariance matrix describes noise shared globally between all voxels in the ROI, and the second term refers to noise specific to individual voxels (with variance τ_i^2 for voxel i). The relative contribution of each of these types of noise is reflected in ρ . The third term models tuning-dependent noise—that is, noise (with variance σ^2) shared between voxels with similar orientation preference.

The generative distribution of voxel responses is thus given by a multivariate normal distribution with mean $\mathbf{W}\mathbf{f}(s)$ and covariance Ω :

$$p(\mathbf{b}|s; \theta) = \mathcal{N}(\mathbf{W}\mathbf{f}(s), \Omega) \quad (6)$$

where $\theta = \{\mathbf{W}, \boldsymbol{\tau}, \rho, \sigma\}$ are the model's parameters. The model's parameters were estimated in a two-step procedure (see ref. ¹⁰ for further details). First, the tuning weights \mathbf{W} were estimated by ordinary least squares regression. Second, the noise covariance parameters ($\rho, \sigma, \boldsymbol{\tau}$) were estimated by numerical maximization of their likelihood.

Model training and testing ('decoding') was performed following a leave-one-run-out cross-validation procedure to prevent double-dipping²⁹. That is, the model parameters were first fit to a training dataset consisting of all but one fMRI run, and the model was then tested on the data from the remaining run. This procedure was repeated until all runs had served as a test set once.

Using the fitted parameters, a posterior distribution over stimulus orientation was computed for each trial in the test set. The posterior distribution is given by Bayes's rule:

$$p(s|\hat{\mathbf{b}}; \hat{\theta}) = \frac{p(\hat{\mathbf{b}}|s; \hat{\theta})p(s)}{\int p(\hat{\mathbf{b}}|s; \hat{\theta})p(s)ds} \quad (7)$$

where $\hat{\theta}$ are the estimated model parameters. The stimulus prior $p(s)$ was flat, given that the stimuli presented in the experiment were uniformly distributed, and the normalizing constant in the denominator was calculated numerically. The circular mean of the posterior distribution was taken as the estimate of the presented orientation on that test trial, and the squared circular standard deviation was used as a measure of the amount of uncertainty in this estimate.

Statistical procedures. Most of our analyses relied on the computation of a correlation coefficient between two variables. These coefficients were calculated for each individual participant and then averaged across observers (see below). On the basis of the assumed relationship between the two variables (linear or monotonic), either Pearson's or Spearman's (rank) correlation coefficient was computed. For the analyses using Pearson's correlation coefficient (Fig. 3a and Extended Data Fig. 2c,d), the data were visually inspected and appeared to be normally distributed, although this was not formally tested. Decoding accuracy was quantified by computing the circular analogue of the Pearson correlation coefficient between the presented and decoded stimulus orientations. To test for an oblique effect in decoded uncertainty, we first calculated for each presented stimulus orientation its distance to the nearest cardinal (that is, horizontal or vertical) orientation and then computed the Spearman correlation coefficient between this measure and decoded uncertainty. To test the relationship between reported confidence and decoded uncertainty (independent of stimulus orientation), we first removed orientation-dependent shifts in decoded uncertainty and confidence by modelling confidence (decoded uncertainty) as a quadratic (linear) function of distance to cardinal (see Extended Data Fig. 3 for the fitted functions); the rank correlation coefficient between confidence and decoded uncertainty was subsequently computed on the residuals of these fitted functions. After we obtained correlation coefficients for each individual observer i , the coefficients were Fisher transformed, and a weighted average was computed across observers. Specifically, the weight of the i th correlation coefficient was calculated as $w_i = 1/v_i$, where v_i is the variance of the Fisher-transformed correlation coefficient⁶². For the Pearson correlation, v_i is given by $1/(n_i - 3)$ (where n_i is the number of trials), and for the Spearman correlation, $v_i = 1.06/(n_i - 3)$ (ref. ⁶³). Weights were adjusted for the additional degrees of freedom lost due to stepwise correction for the oblique effect in decoded

uncertainty or reported confidence by subtracting 1 (for linear correction) or 2 (for quadratic correction) from the denominator in the variance term. The significance of the coefficients was assessed using a Z-test, testing specifically for effects in the direction predicted by the ideal observer models. The average of the Z-transformed values was translated back to the correlation scale for reporting purposes. To compare correlation coefficients between confidence and decoded uncertainty with and without correction for stimulus orientation, we computed Cohen's q and used a Z-test to assess statistical significance. Similar procedures were used for the control analyses in Extended Data Fig. 5. For these control analyses, we additionally performed equivalence tests (using the two one-sided tests procedure⁶⁴), comparing against a smallest effect size of interest of $\rho = 0.1$ (see ref. ⁶⁵ for further rationale).

Some of our analyses required the computation of a dispersion measure (that is, behavioural variability). For these analyses, each participant's data were first divided into ten equal-sized bins, on the basis of either the reported level of confidence or decoded uncertainty, and summary statistics were computed across all trials in a given bin. Behavioural variability was computed as the squared circular standard deviation of (bias-corrected) estimation errors across all trials in each bin, and the average level of confidence or decoded uncertainty was quantified by computing the statistical mean. To test the relationship between behavioural variability and confidence (or decoded uncertainty), we used a multiple linear regression analysis. The independent variables were the level of confidence (or decoded uncertainty) and the absolute distance between the stimulus and the nearest cardinal axis (mean across trials in each bin). We also included participant-specific intercepts. The dependent variable was behavioural variability. Partial correlation coefficients were computed from the binned data, and significance was assessed using t -tests, testing for effects in the direction predicted by the ideal observer models. Control analyses verified that our results did not strongly depend on the number of used bins or on the specific shape of the function used to model the effect of stimulus orientation on confidence (or decoded uncertainty).

Univariate analyses (whole-brain and ROI-based). Whole-brain analysis.

To identify brain regions that are modulated by sensory uncertainty, we used a whole-brain GLM approach. A GLM can be written as $y = X\beta + \epsilon$, where y represents the time series of a single voxel, X is referred to as the design matrix (or model), β is a vector of model parameters and ϵ represents the residuals.

We constructed a model of task-related activity based on three components: (1) a 1.5-s boxcar function time-locked to the stimulus onsets of all excluded trials, with height one; (2) a 1.5-s boxcar function time-locked to the stimulus onsets of all included trials, with height one; and (3) a 1.5-s boxcar function time-locked to the stimulus onsets of all included trials, with its height equal to the decoded uncertainty on that trial (linearly corrected for trial-by-trial differences in stimulus orientation; 'Multivariate analysis (visual cortex)'). Each boxcar function was convolved with a canonical haemodynamic response function and temporal and dispersion derivatives of the haemodynamic response function (SPM's informed basis set), yielding a total of nine regressors to include in the design matrix. The derivatives were added for additional model flexibility regarding the shape and latency of the BOLD response. In addition to the task-related regressors, we included nuisance regressors (24 motion regressors and 2 CSF/WM regressors per session) and run-specific intercepts ('Preprocessing of MRI data') to improve the overall model fit.

The model X was fit to each participant's time series, separately for each voxel, to obtain a set of parameter estimates β . Participant-level analyses were performed using SPM12, because of its increased efficiency (relative to FSL) when performing the GLM analysis on concatenated data rather than individual runs. The resulting participant-level β maps were then transformed from participant-specific to standard space (MNI152) to allow for comparison and combination of estimates across participants. We were specifically interested in the effect of decoded uncertainty on the BOLD response, which was modelled by the three regressors corresponding to the third boxcar function. The combined explanatory power of the three regressors was quantified by computing an F statistic over the corresponding β estimates (across participants). To calculate P values, a sign-flip test (5,000 permutations) was performed in combination with threshold-free cluster enhancement (TFCE)⁶⁶, using FSL's *randome*⁶⁷. The FWER was controlled by comparing the true voxel-wise TFCE scores against the null distribution of the maximum TFCE score across voxels^{66,68}.

ROI analysis. Brain regions modulated by perceptual uncertainty were selected and further investigated as follows. ROIs were defined using existing anatomical atlases, combined with a functional parcellation based on the whole-brain GLM analysis (as described in more detail above). Specifically, within a given (anatomical) ROI, we selected voxels modulated by decoded uncertainty using the GLM analysis, while applying a leave-one-participant-out procedure³⁰ to avoid double-dipping²⁹. This led to the definition of eight ROIs for each participant individually: (1) dAI (using the functional parcellation by Chang et al.²⁶, mirrored to obtain bilateral labels, retrieved from Neurovault: <https://identifiers.org/neurovault.collection:13>), (2) left rPFC (frontal pole label, Harvard–Oxford cortical atlas²⁸, trimmed to include the left hemisphere only), (3) dACC (bilateral RCZa and RCZp labels, Neubert cingulate orbitofrontal connectivity-based parcellation²⁷), (4) precuneus (precuneus label, Harvard–Oxford cortical atlas²⁸), (5) supplementary motor area

(SMA label, Sallet dorsal frontal connectivity-based parcellation⁶⁹, mirrored to obtain bilateral labels), (6) dorsal perigenual anterior cingulate cortex (bilateral area 32d, Neubert cingulate orbitofrontal connectivity-based parcellation²⁷), (7) ventral posterior cingulate cortex (bilateral area 23ab labels, Neubert cingulate orbitofrontal connectivity-based parcellation²⁷) and (8) dorsal posterior cingulate cortex (bilateral CCZ labels, Neubert cingulate orbitofrontal connectivity-based parcellation²⁷). For ROIs 2 and 8, some of the leave-one-out, GLM-based masks did not contain any voxels. The corresponding data were excluded from further analyses for the respective ROIs (for ROI 2, one participant; for ROI 8, two participants). The BOLD signal was averaged over all voxels within a given ROI.

Having defined our ROIs, we then proceeded to investigate the effects of confidence in these regions. We did this in two different analyses. To assess the degree to which confidence modulated the BOLD response in each ROI, we performed a GLM analysis. The model structure was similar to the whole-brain univariate analysis, including three 1.5-s boxcar functions time-locked to stimulus onset: one for excluded trials (height one), one for included trials (height one) and one to model the effect of confidence (included trials only; height equal to confidence value on that trial, quadratically corrected for trial-by-trial differences in stimulus orientation; 'Multivariate analysis (visual cortex)'). These boxcar functions were each convolved with SPM's informed basis set (canonical haemodynamic response function and its temporal and dispersion derivatives) and nuisance regressors (24 motion and 2 CSF/WM regressors per session). Run intercepts were also added.

To further investigate the magnitude and directionality of the effects of reported confidence and decoded uncertainty over the course of a trial (without a priori assumptions regarding the shape or timing of the BOLD response), we also performed a trial-by-trial correlation analysis. Specifically, we computed the Spearman correlation coefficient between BOLD intensity and decoded uncertainty or reported confidence for each TR in the trial. Orientation-dependent changes in decoded uncertainty and confidence were first removed by modelling confidence (decoded uncertainty) as a quadratic (linear) function of distance to cardinal ('Multivariate analysis (visual cortex)'), and the correlation coefficient was computed using the residuals of this fit. For the control analyses presented in Extended Data Fig. 7, response time effects in the BOLD signal were removed by modelling BOLD intensity at each time point (relative to stimulus onset) as a linear function of the time it took for the observer to (1) respond to the presented orientation and (2) report confidence on that trial, and the correlation coefficient between BOLD intensity and decoded uncertainty or confidence was computed on the residuals of this fit. For the partial correlation analyses reported in Extended Data Fig. 8, both reported confidence (or decoded uncertainty) and BOLD intensity at each time point were modelled as linear functions of uncertainty (or confidence). The residuals of these fits were used to compute the (Spearman) correlation coefficient between confidence (or uncertainty) and the BOLD signal for each time point. The single-participant correlation coefficients were Fisher transformed, and a weighted average was computed across observers ('Multivariate analysis (visual cortex)'). Statistical significance was assessed using two-tailed permutation tests, in which uncertainty (or confidence) values were permuted across trials (1,000 permutations). To control for multiple comparisons (FWER), we compared against the null distribution of the maximum correlation coefficient across time points ('Whole-brain analysis'). Finally, we tested whether there was a significant difference in latency between the effects of confidence and uncertainty on the BOLD signal in each ROI. To this end, we determined, for each participant individually, the (within-trial) time point at which the correlation coefficient between BOLD and uncertainty (confidence) was most strongly positive (negative). We then performed a paired t -test on these values, comparing between uncertainty and confidence.

To investigate whether activity in downstream areas mediates the relationship between decoded uncertainty and reported confidence, we performed the following analysis. We first modelled both confidence and uncertainty as linear functions of the BOLD signal in a given ROI and at a given (within-trial) time point. We then took the residuals of these model fits and computed the Spearman correlation coefficient between the (residual) uncertainty and confidence values. If the selected ROIs mediate the relationship between uncertainty and confidence, the residual correlation coefficient should be smaller in magnitude than the baseline correlation coefficient between uncertainty and confidence (that is, not controlled for activity in downstream areas; as reported in Fig. 3c). To quantify the mediating effect of the BOLD signal in each ROI at each time point, the single-participant correlation coefficients were Fisher transformed, and we subtracted from these values the (Fisher-transformed) baseline correlation coefficient between uncertainty and confidence. Finally, a weighted average was computed across observers ('Multivariate analysis (visual cortex)'). Statistical significance of the predicted reduction in correlation strength was assessed using a permutation test, in which BOLD values were permuted across all trials (following otherwise similar procedures as for the whole-brain and main ROI-based analyses).

Eye tracking data. Eye tracking data were acquired using an SR Research Eyelink 1000 system for 62 of 64 sessions. For 11 of these sessions, data were collected for 4–12 runs (of a total of 10–13) due to technical difficulties with the eye-tracking system. Gaze position was sampled at 1 kHz. Blinks and saccades were identified using the Eyelink software and removed. Eye fixations shorter than 100 ms in

duration were similarly identified and removed. Any blinks of duration $>1,000$ ms were considered to be artifacts and removed. For some trials, the quality of the eye tracking data was insufficient (as indicated by a high proportion of missing data points). This was identified by computing the percentage of missing (gaze) data points in a time window starting 4.5 s before stimulus onset and ending 4.5 s after stimulus offset, but excluding the stimulus window itself. Trials were excluded from further analysis if the percentage of missing data points within this pre- and post-stimulus window exceeded 50%. On the basis of this criterion, $3.84 \pm 1.69\%$ (mean \pm s.d.) of trials were excluded from further analysis. The data were band-pass filtered using upper and lower period cut-offs of 36 s and 100 ms, respectively. The median gaze position per run was computed and subtracted from all data points within that run. All measures of interest were computed during stimulus presentation only—that is, over the first 1.5 s of each trial. Mean eye position was obtained by first computing the mean x and y coordinates of the gaze data and then taking the absolute distance from this position to the central fixation target. The proportion of blinks was computed as the fraction of time labelled as blinks; this included saccades immediately preceding or following a blink. A break from fixation occurred when the absolute distance between gaze position and the central fixation target was more than 1.5 degrees of visual angle. The proportion of fixation breaks was computed as the fraction of time labelled as such.

Ideal observer models. *Model description.* We implemented three different observer models, which make identical decisions but differ in how they compute confidence from internal signals. Model 1 takes a statistical approach and computes confidence from the degree of imprecision in the orientation judgement. Models 2 and 3 use heuristic strategies: model 2 uses features of the stimulus as a cue to confidence, and model 3 bases confidence on the magnitude of the observed error in the response. We call these the Bayesian, Stimulus heuristics and Response heuristics observers, respectively (see also Fig. 1).

The observer's task is to infer the stimulus from incoming sensory signals. These signals are noisy, so that there is no one-to-one mapping between a given stimulus s and its measurement m . Rather, the relationship between stimulus and measurements is described by a probability distribution $p(m|s)$. We assume that across trials, the sensory measurements follow a (circular) Gaussian distribution centred on the true stimulus s , with variance $\sigma_m^2(s)$:

$$p(m|s) = \frac{1}{Z} \exp\left(-\frac{1}{2\sigma_m^2(s)} \text{angle}(m, s)^2\right) \quad (8)$$

where Z is a normalization constant.

We make a distinction between three sources of measurement noise: stimulus-dependent sensory noise (σ_s^2), stimulus-independent sensory noise ($\sigma_{s_i}^2$) and non-sensory (downstream) noise (σ_n^2). The total amount of measurement noise equals the sum of the three noise components:

$$\sigma_m^2(s) = \sigma_s^2(s) + \sigma_{s_i}^2 + \sigma_n^2 \quad (9)$$

The stimulus-dependent component, σ_s^2 , represents Gaussian noise that varies in magnitude as a function of stimulus orientation. Specifically, human behavioural orientation judgements tend to be more precise for cardinal than oblique orientations^{19,70}, and we model this oblique effect in orientation perception as a rectified sine function²⁰:

$$\sigma_s^2(s) = a \times \left| \sin s \frac{2\pi}{180} \right| \quad (10)$$

where a is the amplitude of the oblique effect. The stimulus-independent component, $\sigma_{s_i}^2$, models any remaining sources of (Gaussian) sensory noise. Its magnitude varies randomly over trials, and we model the across-trial distribution of $\sigma_{s_i}^2$ as a gamma distribution:

$$\sigma_{s_i}^2 \sim \Gamma(\alpha, \beta) \quad (11)$$

where α represents the shape parameter and β represents the rate parameter. Finally, the non-sensory (downstream) noise component, σ_n^2 , is of constant magnitude and captures (Gaussian) noise that arises beyond the initial stages of sensory processing but prior to the decision—for example, when the item is held in working memory or in processing steps downstream of sensory areas V1–V3.

To infer which stimulus probably caused their sensory measurement, the observers use full knowledge of the generative model. Specifically, each observer inverts the generative model using Bayes's rule. Assuming a flat stimulus prior, the posterior distribution is proportional to the likelihood function:

$$p(s|m) \propto p(m|s) \quad (12)$$

All three observer models take the mean of the posterior distribution as their internal sensory estimate \hat{s} of the presented stimulus. This is the optimal solution for a squared-error loss function⁷¹. The observer's internal estimate of orientation is subsequently translated into an overt behavioural (motor) response r . The transformation from internal estimate into a motor response is noisy. The behavioural response r for the observer models is thus given by:

$$r = \hat{s} + \epsilon_r \quad (13)$$

where ϵ_r is a zero-mean (circular) Gaussian noise variable with variance σ_r^2 .

The three model observers differ in how they compute confidence. The Bayesian observer computes confidence as a function of the expected response error. Specifically, this observer assumes a (circular) squared-error loss function and computes confidence as the inverse of the expected loss (equation (1)). Replacing this direct mapping with any other monotonically decreasing function does not qualitatively change any of the predictions for this model. Thus, for the Bayesian observer, confidence is based (in part) on the posterior probability distribution over the stimulus.

The Stimulus heuristics observer uses the estimated orientation of the stimulus as a cue to uncertainty and confidence. That is, this observer knows that behaviour tends to be more precise for cardinal than oblique orientations, and simply exploits this knowledge in their confidence judgements (equation (2)). The function $f(\hat{s})$ takes the shape of the oblique effect (equation (10)):

$$f(\hat{s}) = a \times \left| \sin \hat{s} \frac{2\pi}{180} \right| + E[\sigma_{s_i}^2] \quad (14)$$

The Response heuristics observer bases confidence on the observed error in the motor response. Specifically, the observer simply notices the difference between the overt response r and internal estimate \hat{s} and adjusts confidence accordingly. We quantified confidence for this model observer as the inverse of the squared acute-angle distance between the internal orientation estimate and the external response (equation (3)).

Simulations. We simulated 50,000 trials for each of the three model observers. The stimulus orientations were drawn from a uniform distribution on the interval $[0-179^\circ]$. Sensory measurements were randomly sampled from the generative model as described above (equations (8)–(11)), with $a = 20$, $\sigma_n^2 = 5$, $\alpha = 10$ and $\beta = 1$. The normalization constant Z was computed numerically.

Probabilistic inference proceeded with full knowledge of the parameter values and according to equation (12). Behavioural responses were obtained using equation (13) and with $\sigma_r^2 = 5$. Confidence judgements were obtained using equations (1)–(3) and (14). To obtain a reasonable range of confidence values, a constant (of value 1) was added to the denominator of equation (3). Confidence ratings were z-scored per observer to ensure that they would all fall on the same scale. Sensory uncertainty was quantified as:

$$\sigma_s^2 = \sigma_{s_i}^2 + \sigma_{s_o}^2 \quad (15)$$

The data were preprocessed following the procedures described in 'Behavioural data analysis'. Similar to the empirical analyses, orientation-dependent shifts in confidence judgements, behavioural variability or sensory uncertainty were removed. For data visualization, the simulated data were divided over ten equal-sized bins of increasing confidence (Fig. 2a,b) or sensory uncertainty (Fig. 2c,d), and the mean confidence level, variance of behavioural errors (Fig. 2a,b) and mean level of sensory uncertainty (Fig. 2c,d) were computed across all trials in each bin.

Citation diversity. We quantified the gender balance of works cited in the main text of this paper ($N = 45$, excluding self-citations) by manual gender classification of the first and last authors. Among the cited works, there are 4.4% single-author male, 73.3% male–male, 2.2% male–female, 15.6% female–male and 4.4% female–female publications. The expected proportions computed from publications in five top neuroscience journals (as reported in ref. ⁷²) are 55.3% male–male, 10.2% male–female, 26.2% female–male and 8.3% female–female.

Reporting Summary. Further information on research design is available in the Nature Research Reporting Summary linked to this article.

Data availability

The preprocessed behavioural and fMRI data for individual participants, as well as unthresholded statistical maps from the whole-brain univariate analysis, can be downloaded from <https://doi.org/10.34973/983b-a047>. To protect participant privacy, the raw data are available from the corresponding author upon request. Source data are provided with this paper.

Code availability

All custom code is available from the corresponding author upon request. Custom code for the probabilistic decoding technique can also be found at <https://github.com/jheehelab/>.

Received: 1 May 2021; Accepted: 2 November 2021;
Published online: 20 January 2022

References

1. Pouget, A., Drugowitsch, J. & Kepecs, A. Confidence and certainty: distinct probabilistic quantities for different goals. *Nat. Neurosci.* **19**, 366–374 (2016).

2. Meyniel, F., Sigman, M. & Mainen, Z. F. Confidence as Bayesian probability: from neural origins to behavior. *Neuron* **88**, 78–92 (2015).
3. Hangya, B., Sanders, J. I. & Kepecs, A. A mathematical framework for statistical decision confidence. *Neural Comput.* **28**, 1840–1858 (2016).
4. Mamassian, P. Visual confidence. *Annu. Rev. Vis. Sci.* **2**, 459–481 (2016).
5. Kepecs, A. & Mainen, Z. F. A computational framework for the study of confidence in humans and animals. *Phil. Trans. R. Soc. B* **367**, 1322–1337 (2012).
6. Sanders, J. I., Hangya, B. & Kepecs, A. Signatures of a statistical computation in the human sense of confidence. *Neuron* **90**, 499–506 (2016).
7. Barthelmé, S. & Mamassian, P. Flexible mechanisms underlie the evaluation of visual confidence. *Proc. Natl Acad. Sci. USA* **107**, 20834–20839 (2010).
8. Adler, W. T. & Ma, W. J. Comparing Bayesian and non-Bayesian accounts of human confidence reports. *PLoS Comput. Biol.* **14**, e1006572 (2018).
9. Denison, R. N., Adler, W. T., Carrasco, M. & Ma, W. J. Humans incorporate attention-dependent uncertainty into perceptual decisions and confidence. *Proc. Natl Acad. Sci. USA* **115**, 11090–11095 (2018).
10. van Bergen, R. S., Ji Ma, W., Pratte, M. S. & Jehee, J. F. M. Sensory uncertainty decoded from visual cortex predicts behavior. *Nat. Neurosci.* **18**, 1728–1730 (2015).
11. Navajas, J. et al. The idiosyncratic nature of confidence. *Nat. Hum. Behav.* **1**, 810–818 (2017).
12. Bertana, A., Chetverikov, A., van Bergen, R. S., Ling, S. & Jehee, J. F. M. Dual strategies in human confidence judgments. *J. Vis.* **21**, 21 (2021).
13. Honig, M., Ma, W. J. & Fougner, D. Humans incorporate trial-to-trial working memory uncertainty into rewarded decisions. *Proc. Natl Acad. Sci. USA* **117**, 8391–8397 (2020).
14. Kepecs, A., Uchida, N., Zariwala, H. A. & Mainen, Z. F. Neural correlates, computation and behavioural impact of decision confidence. *Nature* **455**, 227–231 (2008).
15. Masset, P., Ott, T., Lak, A., Hirokawa, J. & Kepecs, A. Behavior- and modality-general representation of confidence in orbitofrontal cortex. *Cell* **182**, 112–126.e18 (2020).
16. Kiani, R. & Shadlen, M. N. Representation of confidence associated with a decision by neurons in the parietal cortex. *Science* **324**, 759–764 (2009).
17. Green, D. M. & Swets, J. A. *Signal Detection Theory and Psychophysics* (Wiley, 1966).
18. van Bergen, R. S. & Jehee, J. F. M. Modeling correlated noise is necessary to decode uncertainty. *NeuroImage* **180**, 78–87 (2018).
19. Appelle, S. Perception and discrimination as a function of stimulus orientation: the “oblique effect” in man and animals. *Psychol. Bull.* **78**, 266–278 (1972).
20. Girshick, A. R., Landy, M. S. & Simoncelli, E. P. Cardinal rules: visual orientation perception reflects knowledge of environmental statistics. *Nat. Neurosci.* **14**, 926–932 (2011).
21. Goris, R. L. T., Movshon, J. A. & Simoncelli, E. P. Partitioning neuronal variability. *Nat. Neurosci.* **17**, 858–865 (2014).
22. Singer, T., Critchley, H. D. & Preusschoff, K. A common role of insula in feelings, empathy and uncertainty. *Trends Cogn. Sci.* **13**, 334–340 (2009).
23. Behrens, T. E. J., Woolrich, M. W., Walton, M. E. & Rushworth, M. F. S. Learning the value of information in an uncertain world. *Nat. Neurosci.* **10**, 1214–1221 (2007).
24. Rushworth, M. F. S. & Behrens, T. E. J. Choice, uncertainty and value in prefrontal and cingulate cortex. *Nat. Neurosci.* **11**, 389–397 (2008).
25. Fleming, S. M. & Dolan, R. J. The neural basis of metacognitive ability. *Phil. Trans. R. Soc. B* **367**, 1338–1349 (2012).
26. Chang, L. J., Yarkoni, T., Khaw, M. W. & Sanfey, A. G. Decoding the role of the insula in human cognition: functional parcellation and large-scale reverse inference. *Cereb. Cortex* **23**, 739–749 (2013).
27. Neubert, F.-X., Mars, R. B., Sallet, J. & Rushworth, M. F. S. Connectivity reveals relationship of brain areas for reward-guided learning and decision making in human and monkey frontal cortex. *Proc. Natl Acad. Sci. USA* **112**, E2695–E2704 (2015).
28. Desikan, R. S. et al. An automated labeling system for subdividing the human cerebral cortex on MRI scans into gyral based regions of interest. *NeuroImage* **31**, 968–980 (2006).
29. Kriegeskorte, N., Simmons, W. K., Bellgown, P. S. & Baker, C. I. Circular analysis in systems neuroscience: the dangers of double dipping. *Nat. Neurosci.* **12**, 535–540 (2009).
30. Esterman, M., Tamber-Rosenau, B. J., Chiu, Y. C. & Yantis, S. Avoiding non-independence in fMRI data analysis: leave one subject out. *NeuroImage* **50**, 572–576 (2010).
31. Gold, J. I. & Shadlen, M. N. The neural basis of decision making. *Annu. Rev. Neurosci.* **30**, 535–574 (2007).
32. De Martino, B., Fleming, S. M., Garrett, N. & Dolan, R. J. Confidence in value-based choice. *Nat. Neurosci.* **16**, 105–110 (2013).
33. Stolyarova, A. et al. Contributions of anterior cingulate cortex and basolateral amygdala to decision confidence and learning under uncertainty. *Nat. Commun.* **10**, 4704 (2019).
34. van Bergen, R. S. & Jehee, J. F. M. Probabilistic representation in human visual cortex reflects uncertainty in serial decisions. *J. Neurosci.* **39**, 8164–8176 (2019).
35. Walker, E. Y., Cotton, R. J., Ma, W. J. & Tolias, A. S. A neural basis of probabilistic computation in visual cortex. *Nat. Neurosci.* **23**, 122–129 (2020).
36. Fleming, S. M., Huijgen, J. & Dolan, R. J. Prefrontal contributions to metacognition in perceptual decision making. *J. Neurosci.* **32**, 6117–6125 (2012).
37. Grinband, J., Hirsch, J. & Ferrera, V. P. A neural representation of categorization uncertainty in the human brain. *Neuron* **49**, 757–763 (2006).
38. Yoshida, W. & Ishii, S. Resolution of uncertainty in prefrontal cortex. *Neuron* **50**, 781–789 (2006).
39. Karlsson, M. P., Tervo, D. G. R. & Karpova, A. Y. Network resets in medial prefrontal cortex mark the onset of behavioral uncertainty. *Science* **338**, 135–139 (2012).
40. Kolling, N., Behrens, T. E. J., Mars, R. B. & Rushworth, M. F. S. Neural mechanisms of foraging. *Science* **335**, 95–98 (2012).
41. Kolling, N. et al. Value, search, persistence and model updating in anterior cingulate cortex. *Nat. Neurosci.* **19**, 1280–1285 (2016).
42. Shenhav, A., Cohen, J. D. & Botvinick, M. M. Dorsal anterior cingulate cortex and the value of control. *Nat. Neurosci.* **19**, 1286–1291 (2016).
43. Bang, D., Ershadmanesh, S., Nili, H. & Fleming, S. M. Private-public mappings in human prefrontal cortex. *eLife* **9**, e56477 (2020).
44. Morales, J., Lau, H. C. & Fleming, S. M. Domain-general and domain-specific patterns of activity supporting metacognition in human prefrontal cortex. *J. Neurosci.* **38**, 3534–3546 (2018).
45. Shekhar, M. & Rahnev, D. Distinguishing the roles of dorsolateral and anterior PFC in visual metacognition. *J. Neurosci.* **38**, 5078–5087 (2018).
46. Shin, H., Zou, Q. & Ma, W. J. The effects of delay duration on visual working memory for orientation. *J. Vis.* **17**, 10 (2017).
47. Harrison, S. A. & Tong, F. Decoding reveals the contents of visual working memory in early visual areas. *Nature* **458**, 632–635 (2009).
48. Rademaker, R. L., Chunharas, C. & Serences, J. T. Coexisting representations of sensory and mnemonic information in human visual cortex. *Nat. Neurosci.* **22**, 1336–1344 (2019).
49. Li, H.-H., Sprague, T. C., Yoo, A. H., Ma, W. J. & Curtis, C. E. Joint representation of working memory and uncertainty in human cortex. *Neuron* **109**, 3699–3712.e6 (2021).
50. Serences, J. T. Value-based modulations in human visual cortex. *Neuron* **60**, 1169–1181 (2008).
51. Sereno, M. I. et al. Borders of multiple visual areas in humans revealed by functional magnetic resonance imaging. *Science* **268**, 889–893 (1995).
52. Deyoe, E. A. et al. Mapping striate and extrastriate visual areas in human cerebral cortex. *Proc. Natl Acad. Sci. USA* **93**, 2382–2386 (1996).
53. Engel, S. A., Glover, G. H. & Wandell, B. A. Retinotopic organization in human visual cortex and the spatial precision of functional MRI. *Cereb. Cortex* **7**, 181–192 (1997).
54. Kleiner, M., Brainard, D. H. & Pelli, D. G. What's new in Psychtoolbox-3? *Perception* **36** (Suppl.), 14 (2007).
55. Jenkinson, M., Bannister, P., Brady, M. & Smith, S. M. Improved optimization for the robust and accurate linear registration and motion correction of brain images. *NeuroImage* **17**, 825–841 (2002).
56. Reuter, M., Schmansky, N. J., Rosas, H. D. & Fischl, B. Within-subject template estimation for unbiased longitudinal image analysis. *NeuroImage* **61**, 1402–1418 (2012).
57. Smith, S. M. Fast robust automated brain extraction. *Hum. Brain Mapp.* **17**, 143–155 (2002).
58. Smith, S. M. & Brady, J. M. SUSAN—a new approach to low level image processing. *Int. J. Comput. Vis.* **23**, 45–78 (1997).
59. Jenkinson, M., Beckmann, C. F., Behrens, T. E. J., Woolrich, M. W. & Smith, S. M. FSL. *NeuroImage* **62**, 782–790 (2012).
60. Zhang, Y., Brady, M. & Smith, S. M. Segmentation of brain MR images through a hidden Markov random field model and the expectation-maximization algorithm. *IEEE Trans. Med. Imaging* **20**, 45–57 (2001).
61. Brouwer, G. J. & Heeger, D. J. Cross-orientation suppression in human visual cortex. *J. Neurophysiol.* **106**, 2108–2119 (2011).
62. Hedges, L. V. & Olkin, I. *Statistical Methods for Meta-analysis* (Academic Press, 1985).
63. Fieller, E. C. & Pearson, E. S. Tests for rank correlation coefficients: II. *Biometrika* **48**, 29–40 (1961).
64. Schuirman, D. J. A comparison of the two one-sided tests procedure and the power approach for assessing the equivalence of average bioavailability. *J. Pharmacokinet. Biopharm.* **15**, 657–680 (1987).
65. Cohen, J. A power primer. *Psychol. Bull.* **112**, 155–159 (1992).
66. Smith, S. M. & Nichols, T. E. Threshold-free cluster enhancement: addressing problems of smoothing, threshold dependence and localisation in cluster inference. *NeuroImage* **44**, 83–98 (2009).

67. Winkler, A. M., Ridgway, G. R., Webster, M. A., Smith, S. M. & Nichols, T. E. Permutation inference for the general linear model. *NeuroImage* **92**, 381–397 (2014).
68. Nichols, T. E. & Hayasaka, S. Controlling the familywise error rate in functional neuroimaging: a comparative review. *Stat. Methods Med. Res.* **12**, 419–446 (2003).
69. Sallet, J. et al. The organization of dorsal frontal cortex in humans and macaques. *J. Neurosci.* **33**, 12255–12274 (2013).
70. Furmanski, C. S. & Engel, S. A. An oblique effect in human primary visual cortex. *Nat. Neurosci.* **3**, 535–536 (2000).
71. Wei, X. X. & Stocker, A. A. A Bayesian observer model constrained by efficient coding can explain “anti-Bayesian” percepts. *Nat. Neurosci.* **18**, 1509–1517 (2015).
72. Dworkin, J. D. et al. The extent and drivers of gender imbalance in neuroscience reference lists. *Nat. Neurosci.* **23**, 918–926 (2020).
73. Ress, D., Backus, B. T. & Heeger, D. J. Activity in primary visual cortex predicts performance in a visual detection task. *Nat. Neurosci.* **3**, 940–945 (2000).
74. Baird, B., Smallwood, J., Gorgolewski, K. J. & Margulies, D. S. Medial and lateral networks in anterior prefrontal cortex support metacognitive ability for memory and perception. *J. Neurosci.* **33**, 16657–16665 (2013).
75. McCurdy, L. Y. et al. Anatomical coupling between distinct metacognitive systems for memory and visual perception. *J. Neurosci.* **33**, 1897–1906 (2013).
76. Ye, Q., Zou, F., Lau, H., Hu, Y. & Kwok, S. C. Causal evidence for mnemonic metacognition in human precuneus. *J. Neurosci.* **38**, 6379–6387 (2018).
77. Drugowitsch, J., Mendonça, A. G., Mainen, Z. F. & Pouget, A. Learning optimal decisions with confidence. *Proc. Natl Acad. Sci. USA* **116**, 24872–24880 (2019).
78. Kastner, S. et al. Increased activity in human visual cortex during directed attention in the absence of visual stimulation. *Neuron* **22**, 751–761 (1999).
79. Sreenivasan, K. K. & D’Esposito, M. The what, where and how of delay activity. *Nat. Rev. Neurosci.* **20**, 466–481 (2019).

Acknowledgements

We thank A. Sanfey and R. Cools for helpful discussions, C. Beckmann for advice on statistical analyses and P. Gaalman for MRI support. This work was supported by European Research Council Starting Grant No. 677601 (to J.F.M.J.). The funder had no role in study design, data collection and analysis, decision to publish or preparation of the manuscript.

Author contributions

L.S.G., R.S.v.B. and J.F.M.J. conceived and designed the experiments. L.S.G. collected the data. L.S.G. analysed the data, with help from J.F.M.J. L.S.G. and J.R.H.C. constructed the ideal observer models, with help from J.F.M.J. L.S.G., J.R.H.C., R.S.v.B. and J.F.M.J. wrote the manuscript.

Competing interests

The authors declare no competing interests.

Additional information

Extended data is available for this paper at <https://doi.org/10.1038/s41562-021-01247-w>.

Supplementary information The online version contains supplementary material available at <https://doi.org/10.1038/s41562-021-01247-w>.

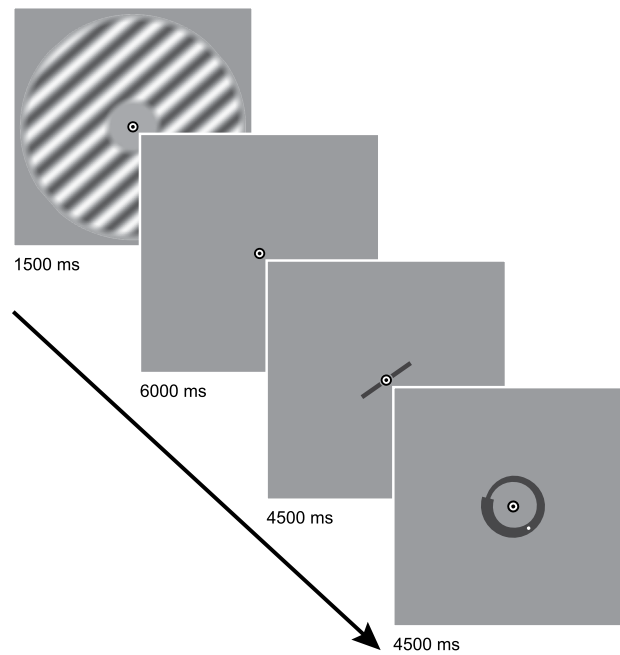
Correspondence and requests for materials should be addressed to Janneke F. M. Jehee.

Peer review information *Nature Human Behaviour* thanks Dan Bang, Pascal Mamassian and Peter Murphy for their contribution to the peer review of this work.

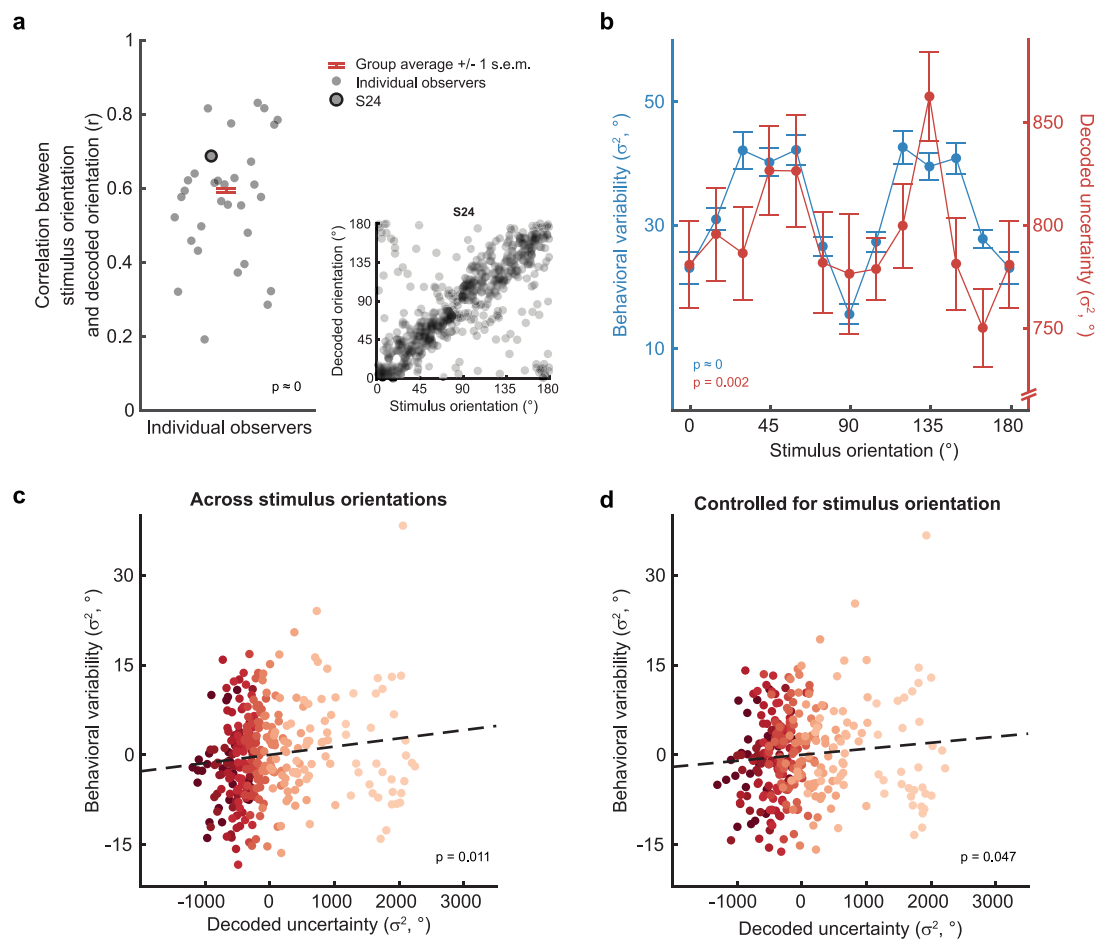
Reprints and permissions information is available at www.nature.com/reprints.

Publisher’s note Springer Nature remains neutral with regard to jurisdictional claims in published maps and institutional affiliations.

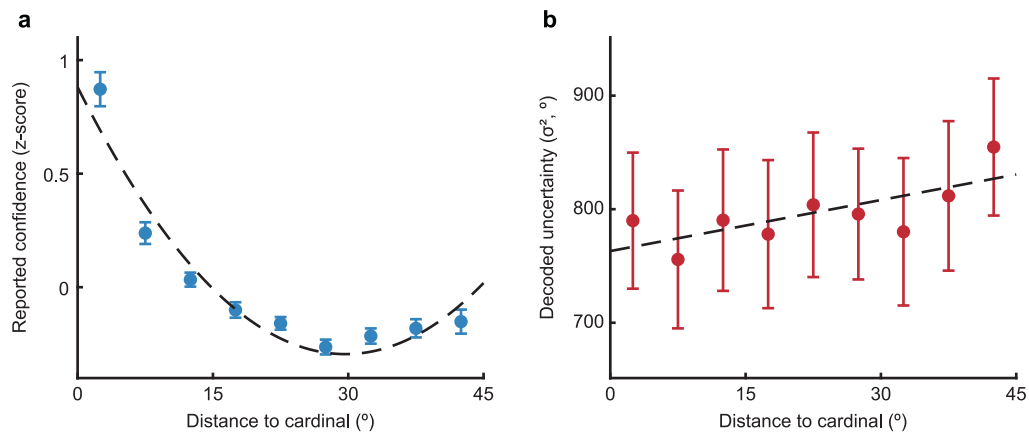
© The Author(s), under exclusive licence to Springer Nature Limited 2022, corrected publication 2022



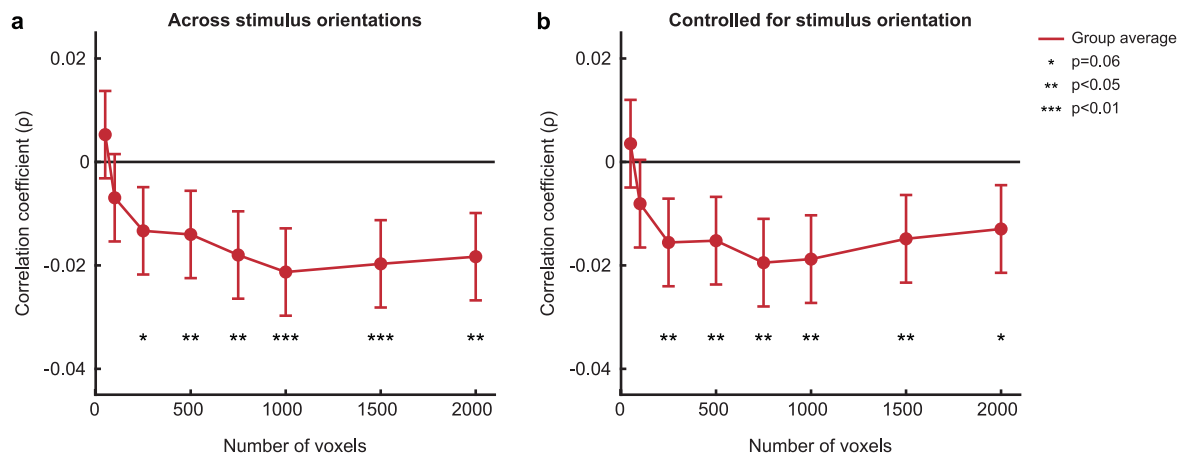
Extended Data Fig. 1 | Trial structure. Each trial started with the presentation of an oriented grating (1500 ms) followed by a 6000-ms fixation interval and two 4500-ms response intervals, during which the participant first reported the orientation of the previously seen stimulus by rotating a bar, and then indicated their level of confidence in this judgment on a continuous scale. Trials were separated by a 1500-ms intertrial interval. Stimulus, response bar and confidence scale are not drawn to their true scale and contrast.



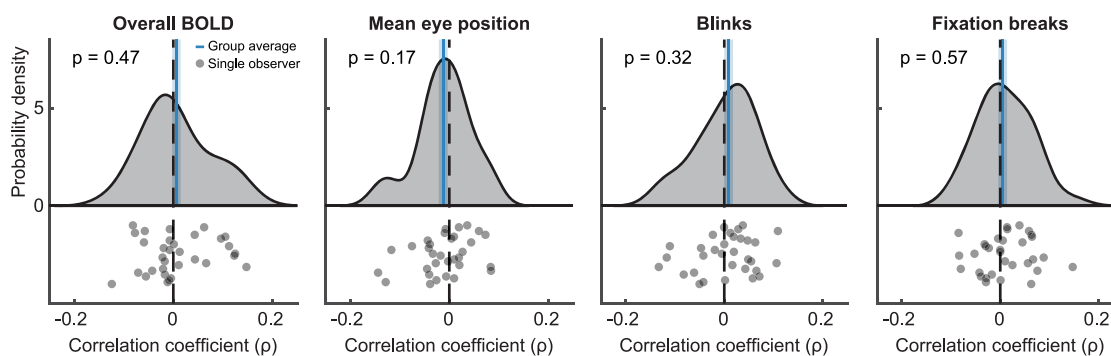
Extended Data Fig. 2 | Orientation and uncertainty decoding performance. The orientation of the presented stimulus, and associated uncertainty, decoded from activity patterns in areas V1-V3. (a) Orientation decoding performance was quantified by means of the circular equivalent of the Pearson correlation coefficient between presented and decoded orientations. Correlation coefficients were computed for each subject individually and then averaged across subjects ($N = 32$). Presented and decoded orientations were significantly correlated ($z = 83.58$, $p < 0.001$, $r = 0.60$, 95% CI = [0.58, 0.61]). (b-d) To assess the degree to which the decoder captured uncertainty contained in neural population activity, we compared decoded uncertainty to behavioral variability, the rationale being that a more precise representation in cortex should also result in more precise behavioral estimates (see also¹⁰). (b) Corroborating our approach, we found that decoded uncertainty was greater for oblique compared to cardinal orientation stimuli (correlation distance-to-cardinal and decoded uncertainty: $z = 2.95$, $p = 0.002$, $p = 0.025$, 95% CI = [0.0083 0.041]). This finding was paralleled by the imprecision in observer behaviour (correlation distance-to-cardinal and behavioral variability: $t(287) = 13.60$, $p < 0.001$, $r = 0.63$, 95% CI = [0.55, 0.69]). (c-d) In addition, behavioral orientation responses were more precise when the decoded probability distributions indicated greater certainty in cortex, (c) both across orientation stimuli (correlation decoded uncertainty and behavioral variability: $t(287) = 2.30$, $p = 0.011$, $r = 0.13$, 95% CI = [0.019, 0.25]), and (d) when controlling for orientation ($t(286) = 1.68$, $p = 0.047$, $r = 0.099$, 95% CI = [-0.017, 0.21]). Altogether, this further underscores the validity of the decoding approach and shows that decoded uncertainty reliably characterizes the degree of imprecision in cortical representations of the stimulus (see^{10,18} for further proof of this approach). Note that these are partial residual plots, which is why the data is centered around 0. Error bars (a-b) represent ± 1 s.e.m. (c-d) Shades of red indicate ten equal-size bins of increasing decoded uncertainty, dots represent individual observers ($N = 32$).



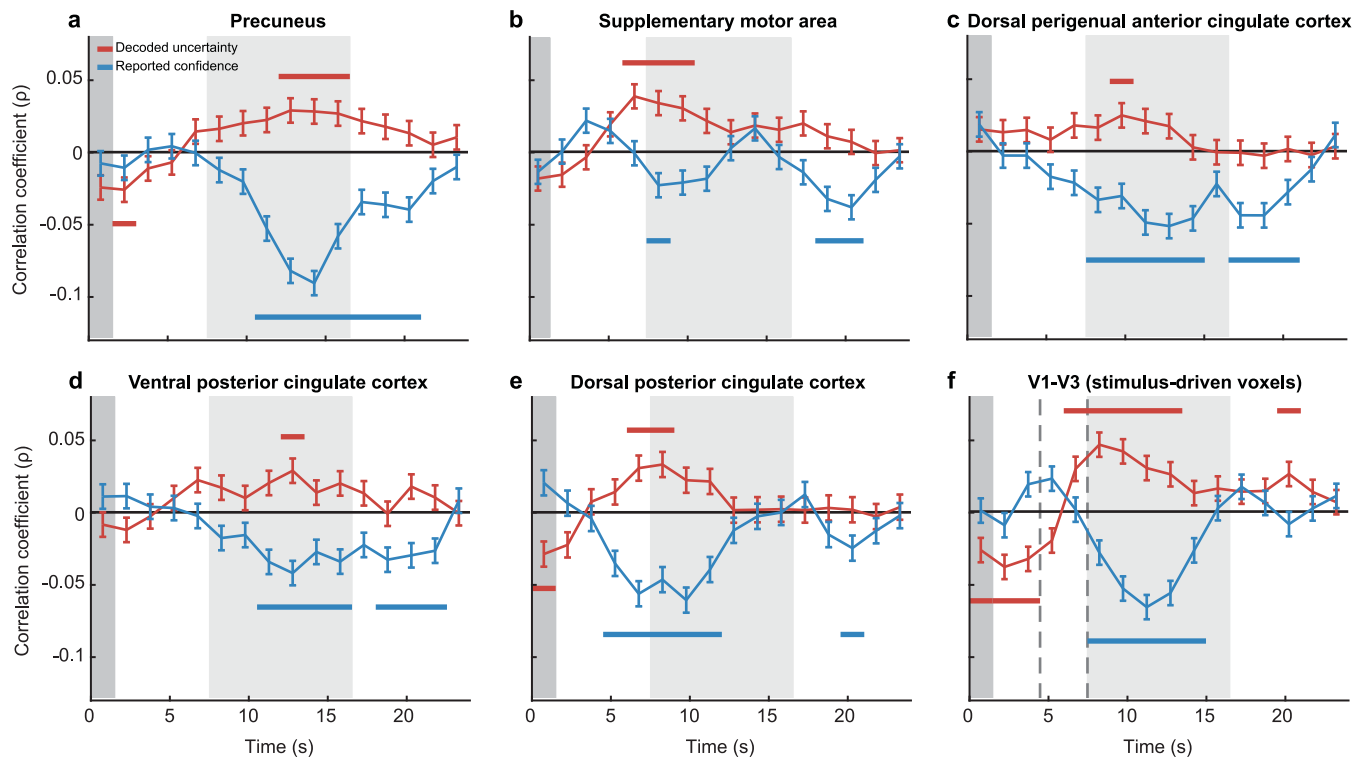
Extended Data Fig. 3 | Oblique effect in reported confidence and decoded uncertainty. Effect of stimulus orientation on reported confidence (**a**) and decoded uncertainty (**b**). Each participant's data were first binned based on the absolute distance between presented stimulus orientation and the nearest cardinal axis (equal-width bins), and then averaged across trials and finally across subjects (error bars represent ± 1 s.e.m.). Dashed lines indicate best-fitting function (least-squares; quadratic for confidence, linear for decoded uncertainty). Functions were fitted on the trial-by-trial data for each participant, and averaged across participants.



Extended Data Fig. 4 | Relationship between decoded uncertainty and reported confidence across different numbers of voxels. Correlation coefficients between decoded uncertainty and reported confidence as a function of the number of voxels included in the ROI, both across all orientations (a) and after removing the effect of stimulus orientation (b). Voxels within V1-V3 were ranked and selected for multivariate analysis based on their response to the visual localizer stimulus (see Methods), using a lenient statistical threshold of $p < 0.01$, uncorrected. The results proved reasonably robust to variations in the number of voxels selected for analysis. Dark red line indicates group average correlation coefficients, error bars denote ± 1 s.e.m.

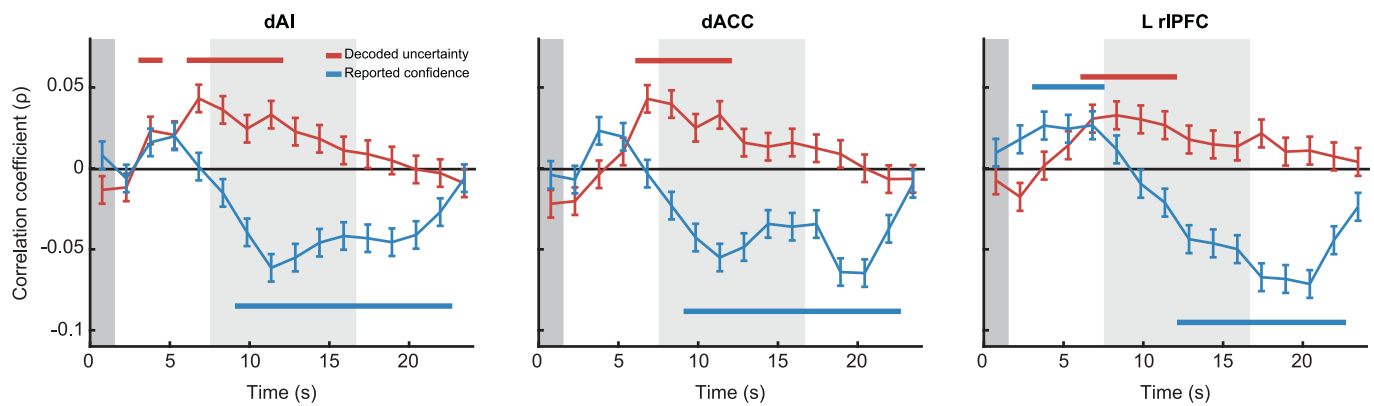


Extended Data Fig. 5 | No effects of overall BOLD or eyetracking measures on confidence. Reported confidence is not significantly correlated with the mean BOLD response to the stimulus in areas V1-V3 ($z=0.73$, $p=0.47$, $\rho=0.0062$, 95% CI=[−0.010, 0.023]; equivalence test: $z=-0.094$, $p<0.001$), nor with mean eye position (mean absolute distance to screen center; $z=-1.38$, $p=0.17$, $\rho=-0.012$, 95% CI=[−0.030, 0.0051]; equivalence test: $z=-0.088$, $p<0.001$), eye blinks ($z=0.99$, $p=0.32$, $\rho=0.0087$, 95% CI=[−0.0086, 0.026]; equivalence test: $z=-0.11$, $p<0.001$), or the number of breaks from fixation during stimulus presentation ($z=0.57$, $p=0.57$, $\rho=0.0050$, 95% CI=[−0.012, 0.022]; equivalence test: $z=-0.11$, $p<0.001$), suggesting that participants did not rely on heuristics in terms of eye position ('did I look at the stimulus?') or eye blinks ('were my eyes closed?') for reporting confidence. It furthermore rules out simple heuristic explanations in terms of attentional effort ('my mind was elsewhere', 'I didn't really try that hard'), as the mean BOLD response to the stimulus tends to increase with attention in these areas⁷³. Shaded blue represents ± 1 s.e.m. Gray dots denote individual observers ($N=32$).

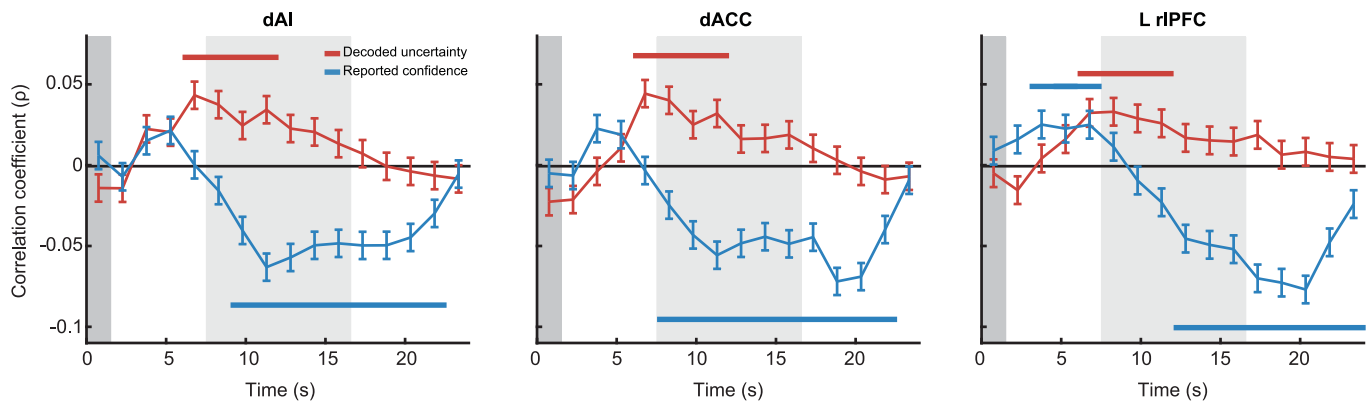


Extended Data Fig. 6 | Effects of decoded uncertainty and reported confidence on the BOLD response in precuneus, supplementary motor area, dorsal perigenual anterior cingulate cortex, ventral posterior cingulate cortex, dorsal posterior cingulate cortex, and stimulus-driven voxels in V1-V3.

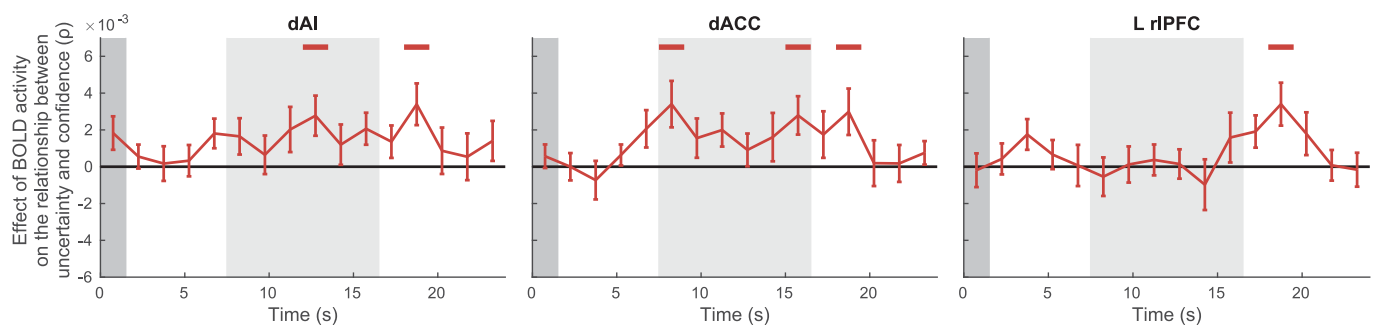
Group-average correlation coefficients for the relationship between decoded uncertainty and BOLD contrast, and reported confidence and BOLD contrast, in six ROIs. **(a)** In precuneus, the effects of both decoded sensory uncertainty and reported confidence on BOLD peaked around the same time, i.e. during the second half of the response window. This finding is consistent with previous work suggesting that precuneus may represent uncertainty in memory but not in perception⁷⁴⁻⁷⁶. **(b)** In supplementary motor area, both decoded uncertainty and reported confidence modulated cortical activity relatively early in the response window, while the effects of confidence lingered until after observers gave their response. **(c-d)** In dorsal perigenual anterior cingulate cortex and ventral posterior cingulate cortex, decoded uncertainty had a moderate effect on the BOLD response. Reported confidence modulated cortical activity during as well as shortly after the response window. **(e)** In dorsal posterior cingulate cortex, the modulatory effect of both decoded uncertainty and reported confidence on the cortical response was largest around the onset of the response window. **(f)** Stimulus-driven voxels in early visual cortex were modulated by both decoded uncertainty and reported confidence, most notably during the first portion of the response interval. Given the timing of the effect (and taking into account the hemodynamic delay), this likely does not reflect uncertainty in the sensory representation *per se*, but is consistent with anticipatory processes or working memory-related signals potentially influenced by the imprecision in the cortical stimulus representation⁷⁷⁻⁷⁹. Please note there is no net effect of uncertainty on the overall (univariate) BOLD response during the decoding window (stimulus presentation; dashed lines). (a-f) Horizontal lines indicate statistical significance ($p < 0.05$, FWER-controlled). Error bars represent ± 1 s.e.m. Dark gray area marks stimulus presentation window, light gray area marks response window.



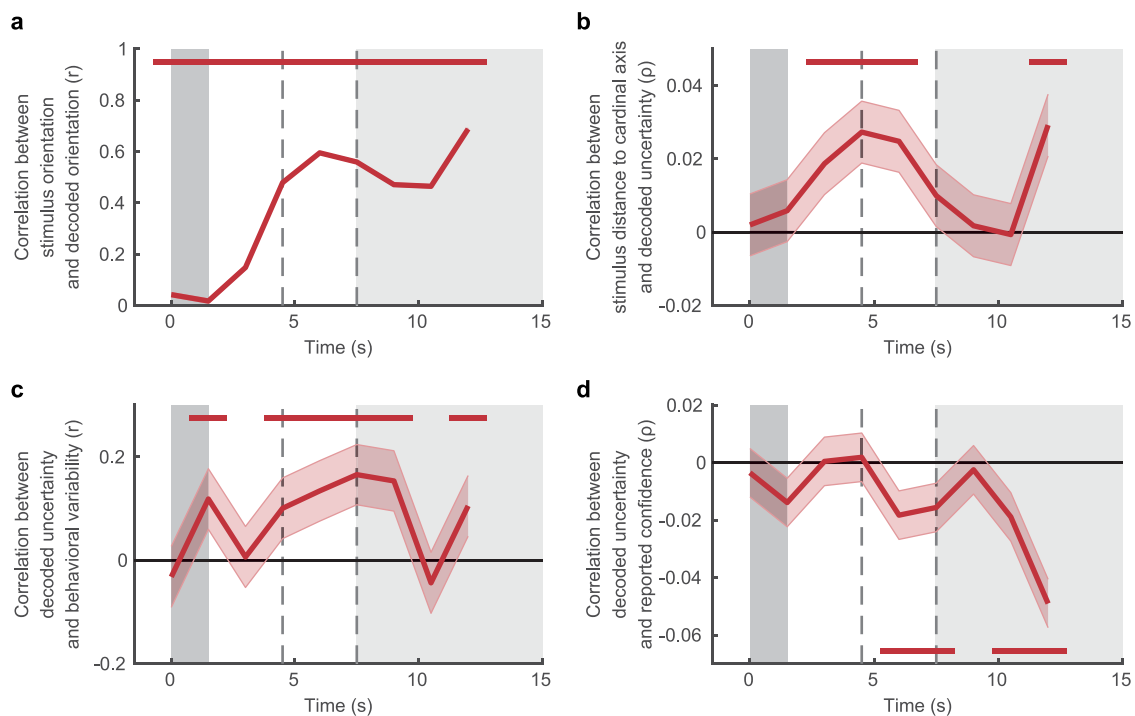
Extended Data Fig. 7 | Effects of decoded uncertainty and reported confidence on the BOLD response in dAI, dACC and rIPFC, after accounting for trial-by-trial fluctuations in behavioral response times. Behavioral response time effects were linearly regressed out from decoded uncertainty and reported confidence, prior to computing the Spearman correlation coefficient between decoded uncertainty (reported confidence) and the BOLD response at different moments in time after stimulus presentation. The remaining analysis steps are identical to those in the main text. Removing the effect of behavioral response time did not qualitatively change the pattern of results in any of these ROIs. Horizontal lines indicate statistical significance ($p < 0.05$, FWER-controlled). Dark gray area marks stimulus presentation window, light gray area denotes response window. Error bars represent ± 1 s.e.m.



Extended Data Fig. 8 | Effects of decoded uncertainty (or reported confidence) on the BOLD response in dAI, dACC and rIPFC, after controlling for confidence (or decoded uncertainty). Reported confidence (or decoded uncertainty) was linearly regressed on both decoded uncertainty (or reported confidence) and the BOLD response at different moments in time after stimulus presentation. The residuals of these fits were then used to compute the group-averaged correlation coefficient between cortical response amplitude and decoded uncertainty (red) or reported confidence (blue). For all ROIs, the results are qualitatively similar to the main results reported in Fig. 4 in the main text. Horizontal lines indicate statistical significance ($p < 0.05$, FWER-controlled). Dark gray area marks stimulus presentation window, light gray area denotes response window. Error bars represent ± 1 s.e.m.



Extended Data Fig. 9 | Activity in dAI, dACC, and left rIPFC mediates the relationship between decoded uncertainty and reported confidence. To assess the degree to which the cortical activity in these regions mediates the observed relationship between decoded uncertainty and reported confidence, we performed the following analysis. We first modeled both uncertainty and confidence as a function of the overall BOLD signal in a given ROI at each timepoint, and then used the residuals of these fits to compute the Spearman correlation coefficient between decoded uncertainty and reported confidence when controlled for the BOLD signal. From the resulting correlation coefficient, we subtracted the (baseline) correlation coefficient that was obtained while we did not control for the BOLD signal (see Fig. 3c). We observed a significant net effect at various moments in time, which indicates that there was a reliable reduction in the strength of the inverse (negative) correlation coefficient between uncertainty and confidence when we controlled for BOLD intensity. This suggests that the level of cortical activity in these windows (partially) mediates the relationship between decoded uncertainty and reported confidence. Horizontal lines indicate statistical significance ($p < 0.05$, FWER-controlled). Dark gray area marks stimulus presentation window, light gray area denotes response window. Dashed lines indicate the decoding window used in the main analyses (Fig. 3b–c and Extended Data Fig. 2). Error bars represent ± 1 s.e.m.



Extended Data Fig. 10 | Decoding results over time. Does reported confidence similarly reflect imprecision in the cortical representation when the orientation is held in visual working memory? To address this question, the analyses of Fig. 3b–c and Extended Data Fig. 2 were repeated over time, using a sliding window of size 3 s (2 TRs). We focused on successive intervals from 1.5 s before to 13.5 s after stimulus onset (which roughly corresponds to the onset of the response window after accounting for hemodynamic delay). Benchmark tests verified that the decoded probability distributions reliably predict the orientation of the presented stimulus (**a**), and variability in the observer’s behavioral estimates (**b–c**) over extended periods of time. Having established that the decoded distributions meaningfully reflect the degree of imprecision in the cortical representation, we next investigated the extent to which decoded uncertainty predicts reported confidence during the retention interval. We found a reliable negative relationship between decoded uncertainty and reported confidence that held up well into the delay period (**d**). This is consistent with an imprecise working memory trace in V1–V3 that influences subjective confidence. Please note, however, that our design does not warrant strong conclusions regarding the nature of this representation: due to fMRI’s low temporal resolution, it is difficult to say whether these signals are purely perceptual or working memory-related (see e.g.⁴⁷ for similar rationale), and later TRs could simply reflect the visual presentation of the response bar, rather than memory-based signals. (a–d) Data are centered to the middle of the analysis window (of size 2 TRs). Horizontal lines indicate statistical significance ($p < 0.05$, FWER-controlled). Dark gray area marks stimulus presentation window, light gray area denotes response window. Dashed lines indicate the decoding window used for the main analyses (i.e., Fig. 3b,c and Extended Data Fig. 2). Shaded regions represent ± 1 s.e.m. (standard errors in (a) are too small to be visible).

Reporting Summary

Nature Research wishes to improve the reproducibility of the work that we publish. This form provides structure for consistency and transparency in reporting. For further information on Nature Research policies, see our [Editorial Policies](#) and the [Editorial Policy Checklist](#).

Statistics

For all statistical analyses, confirm that the following items are present in the figure legend, table legend, main text, or Methods section.

n/a Confirmed

- ☐ ☒ The exact sample size (n) for each experimental group/condition, given as a discrete number and unit of measurement
- ☐ ☒ A statement on whether measurements were taken from distinct samples or whether the same sample was measured repeatedly
- ☐ ☒ The statistical test(s) used AND whether they are one- or two-sided
Only common tests should be described solely by name; describe more complex techniques in the Methods section.
- ☐ ☒ A description of all covariates tested
- ☐ ☒ A description of any assumptions or corrections, such as tests of normality and adjustment for multiple comparisons
- ☐ ☒ A full description of the statistical parameters including central tendency (e.g. means) or other basic estimates (e.g. regression coefficient) AND variation (e.g. standard deviation) or associated estimates of uncertainty (e.g. confidence intervals)
- ☐ ☒ For null hypothesis testing, the test statistic (e.g. F , t , r) with confidence intervals, effect sizes, degrees of freedom and P value noted
Give P values as exact values whenever suitable.
- ☒ ☐ For Bayesian analysis, information on the choice of priors and Markov chain Monte Carlo settings
- ☐ ☒ For hierarchical and complex designs, identification of the appropriate level for tests and full reporting of outcomes
- ☐ ☒ Estimates of effect sizes (e.g. Cohen's d , Pearson's r), indicating how they were calculated

Our web collection on [statistics for biologists](#) contains articles on many of the points above.

Software and code

Policy information about [availability of computer code](#)

Data collection Matlab 2012a

Data analysis Matlab 2018b, SPM12, FSL 6.0.1, freesurfer 5.3, custom code (PRINCE decoding algorithm: <https://github.com/jeheelab/TAFKAP>; see van Bergen et al., 2015, Nature Neuroscience; van Bergen & Jehee, 2018, NeuroImage)

For manuscripts utilizing custom algorithms or software that are central to the research but not yet described in published literature, software must be made available to editors and reviewers. We strongly encourage code deposition in a community repository (e.g. GitHub). See the Nature Research [guidelines for submitting code & software](#) for further information.

Data

Policy information about [availability of data](#)

All manuscripts must include a [data availability statement](#). This statement should provide the following information, where applicable:

- Accession codes, unique identifiers, or web links for publicly available datasets
- A list of figures that have associated raw data
- A description of any restrictions on data availability

The data used to generate the main figures in this article are provided under Source Data. Preprocessed behavioral and fMRI data for individual participants, as well as unthresholded statistical maps from the whole-brain univariate analysis, can be downloaded from: <https://doi.org/10.34973/983b-a047>. To protect participant privacy, the raw data are available from the corresponding author upon request.

Field-specific reporting

Please select the one below that is the best fit for your research. If you are not sure, read the appropriate sections before making your selection.

☒ Life sciences ☐ Behavioural & social sciences ☐ Ecological, evolutionary & environmental sciences

For a reference copy of the document with all sections, see [nature.com/documents/nr-reporting-summary-flat.pdf](https://www.nature.com/documents/nr-reporting-summary-flat.pdf)

Life sciences study design

All studies must disclose on these points even when the disclosure is negative.

Sample size	Sample size (N=32) was based on a power calculation (power = 0.8; alpha = 0.05).
Data exclusions	Trials on which the participant's behavioral error was more than three standard deviations away from the mean of that participant (after bias correction) were marked as guesses and excluded from further analysis (1-7 out of 440-520 trials). Trials on which the participant did not finish their response by the end of the response window were also excluded from further analyses (0-43 out of 440-520 trials).
Replication	We implemented an ideal observer model (i.e., normative computational model). This resulted in a number of quantitative predictions, each of which we experimentally tested in several independent ways. All of our predictions were supported by the empirical data.
Randomization	We used a within-subjects design, so no allocation into experimental groups was necessary.
Blinding	We used a within-subjects design so blinding was not necessary.

Reporting for specific materials, systems and methods

We require information from authors about some types of materials, experimental systems and methods used in many studies. Here, indicate whether each material, system or method listed is relevant to your study. If you are not sure if a list item applies to your research, read the appropriate section before selecting a response.

Materials & experimental systems

n/a	Involved in the study
<input checked="" type="checkbox"/>	<input type="checkbox"/> Antibodies
<input checked="" type="checkbox"/>	<input type="checkbox"/> Eukaryotic cell lines
<input checked="" type="checkbox"/>	<input type="checkbox"/> Palaeontology and archaeology
<input checked="" type="checkbox"/>	<input type="checkbox"/> Animals and other organisms
<input type="checkbox"/>	<input checked="" type="checkbox"/> Human research participants
<input checked="" type="checkbox"/>	<input type="checkbox"/> Clinical data
<input checked="" type="checkbox"/>	<input type="checkbox"/> Dual use research of concern

Methods

n/a	Involved in the study
<input checked="" type="checkbox"/>	<input type="checkbox"/> ChIP-seq
<input checked="" type="checkbox"/>	<input type="checkbox"/> Flow cytometry
<input type="checkbox"/>	<input checked="" type="checkbox"/> MRI-based neuroimaging

Human research participants

Policy information about [studies involving human research participants](#)

Population characteristics	Participants were healthy adults (age range 19-31, 20 female, 12 male) with normal or corrected-to-normal vision. All participants gave informed written consent prior to their participation and received monetary compensation for their participation (8 or 10 euros per hour for behavioral and fMRI sessions, respectively).
Recruitment	Participants were recruited via the participant database (SONA systems) of Radboud University and among colleagues and acquaintances. We compared how well quantitative predictions from different computational models could predict the participant's brain and behavioral data, and it is implausible that the recruitment procedures would benefit any particular one of these models.
Ethics oversight	CMO Arnhem-Nijmegen, the Netherlands

Note that full information on the approval of the study protocol must also be provided in the manuscript.

Magnetic resonance imaging

Experimental design

Design type	Task; slow event-related design
-------------	---------------------------------

Design specifications

Two fMRI sessions per participant. 10-13 runs per session. 20 trials per run (16.5 s/trial + 1.5 s inter-trial interval + 4.5 s fixation at the start of the run and 15 s at the end). Additionally, each scan session included one or two functional localizer runs, in which flickering checkerboard stimuli were presented in seven 12-s blocks interleaved with fixation blocks of equal duration.

Behavioral performance measures

We recorded the position of the orientation bar and the position of the confidence dot, as well as the timing of the first and last button presses, in each response window. Participants generally performed well on the task, with a mean absolute behavioral estimation error of $4.34^\circ \pm 0.212^\circ$ (mean \pm SEM across subjects). In general, participants finished adjusting their orientation and confidence responses well before the end of the response windows (4.5 s each), taking on average 2761 ± 378 ms (mean \pm S.D. across observers) for the orientation response and 2587 ± 313 ms for the confidence response.

Acquisition

Imaging type(s)

Functional, structural

Field strength

3T

Sequence & imaging parameters

For anatomical reference, a high-resolution T1-weighted image was collected at the start of each session (3D MPRAGE, TR: 2300 ms, TI: 1100 ms, TE: 3 ms, flip angle: 8 degrees, FOV: 256 x 256 mm, 192 sagittal slices, 1-mm isotropic voxels). B0 field inhomogeneity maps (TR: 653 ms, TE: 4.92 ms, flip angle: 60 degrees, FOV: 256 x 256 mm, 68 transversal slices, 2-mm isotropic voxels, interleaved slice acquisition) were acquired. Functional data were acquired using a multi-band accelerated gradient-echo EPI protocol, in 68 transversal slices covering the whole brain (TR: 1500 ms, TE: 38.60 ms, flip angle: 75 degrees, FOV: 210 x 210 mm, 2-mm isotropic voxels, multiband acceleration factor: 4, interleaved slice acquisition).

Area of acquisition

Whole brain

Diffusion MRI

☐ Used

☒ Not used

Preprocessing

Preprocessing software

FSL 6.0.1 and freesurfer 5.3 were used for preprocessing of MRI data. Slow drifts in the BOLD signal were removed using FSL's nonlinear high-pass temporal filter (fslmaths) with a sigma of 24 TRs (corresponding to two trials). For univariate analyses only, we additionally removed non-brain structures using FSL's BET (fractional intensity threshold: 0.2), and spatially smoothed the data with a 6-mm Gaussian kernel using FSL's SUSAN. FSL's MCFLIRT was used for motion correction. FSL's FLIRT was applied to unwarp EPI data (using a field map obtained in the same session), and to register the unwarp data to the within-session anatomical reference image.

Normalization

For univariate analyses, each subject's anatomical template (created with freesurfer's mri_robust_template) was non-linearly registered to MNI152 space using FSL's FNIRT with a warp resolution of 10 mm isotropic. For multivariate analyses, the data were analyzed within subjects, so no normalization was necessary.

Normalization template

Univariate analyses: MNI152
Multivariate analyses: n/a

Noise and artifact removal

The following nuisance regressors were used: an intercept regressor per run, 24 motion regressors based on the transformation parameters obtained from the motion correction algorithm (all analyses), and two regressors reflecting the average signal in cerebrospinal fluid (CSF) and white matter (WM) (univariate analyses only). Motion regressors included raw displacement parameters (3 rotations + 3 translations), the displacement parameters squared, their temporal derivatives, and gradients. The CSF and WM regressors served to capture global fluctuations in signal intensity and were obtained by first creating WM and CSF masks based on the subject's anatomical scan data using FSL's FAST, and then removing the outer edges from these masks to exclude voxels at the tissue boundaries. For the multivariate and ROI-based univariate analyses, nuisance signals were removed from the BOLD signal prior to further analyses, and no further artifact removal was applied. For the whole-brain univariate analysis, motion, CSF/WM, and intercept regressors were included as covariates in the general linear model.

Volume censoring

No volume censoring was performed.

Statistical modeling & inference

Model type and settings

We performed both multivariate and univariate (whole-brain and ROI-based) analyses.

Multivariate analyses were based on a previously published, generative-model based decoding technique (van Bergen et al., 2015, Nature Neuroscience; van Bergen & Jehee, 2018, Neurolmage). Using this technique, and for each individual subject, we extracted from BOLD activity a probability distribution over stimulus orientation on a trial-by-trial basis. 'Decoded uncertainty' was quantified as the squared circular standard deviation of the decoded distribution.

For the whole-brain univariate analyses, the following model was fit to single-subject multi-session, concatenated data (using SPM12). 1) a 1.5-s boxcar function time-locked to the stimulus onsets of all excluded trials, with height one, 2) a 1.5-s boxcar function time-locked to the stimulus onsets of all included trials, with height one, 3) a 1.5-s boxcar function time-locked to the stimulus onsets of all included trials, with its height equal to the level of sensory uncertainty on that trial (decoded from activity in visual cortex, and linearly corrected for trial-by-trial differences in stimulus orientation). Each boxcar function was

convolved with a canonical hemodynamic response function (HRF) and temporal and dispersion derivatives of the HRF (SPM's informed basis set), yielding a total of nine regressors to include in the design matrix. We furthermore included nuisance regressors (24 motion regressors and 2 CSF/WM regressors per session), and run-specific intercepts (see also above). Permutation tests were used to assess statistical significance at the group level (see below).

For the ROI-based univariate analyses, two types of analyses were performed. First, a GLM was fitted using identical procedures as described above, except that for component 3) decoded uncertainty values were replaced by the level of confidence reported by the participant on that trial. Second, we performed a trial-by-trial correlation analysis. Specifically, for each individual participant and for each TR in the trial, we computed the Spearman correlation coefficient between BOLD intensity and decoded uncertainty or reported confidence (after removing orientation-dependent changes in decoded uncertainty and confidence, see Methods for further details). The single-subject correlation coefficients were Fisher transformed, and a weighted average was computed across observers. Statistical significance was assessed using permutation tests.

Effect(s) tested

Multivariate analyses: we tested the relationship between decoded uncertainty and behavioral variability (variance of response errors), both corrected and uncorrected for differences in presented stimulus orientation, using multiple linear regression. We tested the relationship between reported confidence and decoded uncertainty (trial-by-trial), using rank regression. We ran benchmark tests for our decoding approach, testing the relationship between decoded and presented stimulus orientation (circular correlation), between decoded uncertainty and stimulus distance to cardinal (rank regression), and between decoded uncertainty and behavioral variability (linear regression).

Whole-brain univariate analyses: we tested the trial-by-trial relationship between decoded uncertainty and BOLD activity by computing (across subjects) an F-statistic over the beta estimates corresponding to the three regressors derived from the third model component as described above (i.e., 1.5-s boxcar function time-locked to the stimulus onset of included trials, with its height equal to decoded uncertainty on that trial).

ROI-based univariate analyses: we tested the overall trial-by-trial relationship between reported confidence and BOLD activity by computing (across subjects) an F-statistic over the beta estimates corresponding to the three regressors derived from the third model component (i.e., 1.5-s boxcar function time-locked to the stimulus onset of included trials, with its height equal to reported confidence on that trial). We additionally tested the trial-by-trial relationship between BOLD activity and decoded uncertainty or reported confidence for each TR in the trial separately, using rank regression.

Specify type of analysis: ☐ Whole brain ☐ ROI-based ☒ Both

Multivariate analyses: areas V1, V2, and V3 were manually identified on the reconstructed cortical surface, based on retinotopic maps acquired using standard retinotopic mapping procedures in a separate scan session.

Anatomical location(s)

ROI-based univariate analyses: ROIs were defined using existing anatomical atlases, combined with a functional parcellation based on the whole-brain GLM analysis. Specifically, within a given (anatomical) ROI, we selected voxels modulated by decoded uncertainty in the whole-brain GLM analysis, while applying a leave-one-subject-out procedure to avoid double-dipping. The specific atlases used for individual ROIs are further detailed in the Methods section.

Statistic type for inference (See [Eklund et al. 2016](#))

Multivariate analyses: based on the assumed relationship between the two variables (linear or monotonic), linear or rank correlation coefficients were computed. Correlation coefficients were Fisher-transformed and then averaged across participants, after which statistical significance was assessed using a Z-test. For analyses that required binning of data, multiple linear regression (across-subjects) was used, and statistical significance of partial correlation coefficients was assessed using a t-test.

Univariate whole-brain analyses: To calculate p-values, a sign-flip test (5000 permutations; voxelwise) was performed in combination with threshold-free cluster enhancement (TFCE), using FSL's randomise.

ROI-based univariate analyses: To assess the overall effect of confidence, we used identical procedures as for the univariate whole-brain analyses. For the TR-wise analyses, statistical significance was assessed using permutation tests, in which uncertainty (or confidence) values were permuted across trials (1000 permutations).

Correction

Multivariate analyses: n/a

Univariate whole-brain analyses & ROI-based univariate analyses (overall effect of confidence): The family-wise error rate (FWER) was controlled by comparing the true voxel-wise TFCE scores against the null distribution of the maximum TFCE score across voxels.

ROI-based univariate analyses (TR-wise): To control for multiple comparisons (FWER) we compared against the null distribution of the maximum correlation coefficient across timepoints (obtained through permutation testing).

Models & analysis

n/a | Involved in the study

- ☒ ☐ Functional and/or effective connectivity
☒ ☐ Graph analysis
☐ ☒ Multivariate modeling or predictive analysis

Multivariate modeling and predictive analysis

We made use of a previously published, generative-model based, probabilistic decoding technique (van

Bergen et al., 2015, Nature Neuroscience; van Bergen & Jehee, 2018, NeuroImage; code available here: <https://github.com/jeheelab/TAFKAP>). From samples of BOLD activity, we extracted a probability distribution over orientation. Within the ROI (areas V1, V2, and V3, combined), we selected the 2000 voxels that were activated most strongly by the functional localizer stimulus while surviving a lenient statistical threshold ($p < 0.01$, uncorrected). The time series of each selected voxel was subsequently z-normalized with respect to corresponding trial time points in the same run. Activation patterns for each trial were obtained by averaging over the first 3 s of each trial, after adding a 4.5 s temporal shift to account for hemodynamic delay. A leave-one-run-out cross-validation procedure was used for model training and testing. The independent variable (for training) was the presented stimulus orientation.

We used a previously published and well-validated approach (van Bergen et al., 2015, Nature Neuroscience; van Bergen & Jehee, 2018, NeuroImage). Additional benchmark analyses verified that 1) orientation decoding performance was well above chance levels, 2) decoded uncertainty was lower for cardinal compared to oblique orientation stimuli, and 3) decoded uncertainty predicted behavioral variability, both within and across stimulus orientations. This replicates van Bergen et al. (2015) and confirms that the precision of the observer's internal sensory evidence was reliably extracted from the patterns of fMRI activity on a trial-by-trial basis.